

Chapter 3: Manipulation and detection of ultra-cold atoms

All of the experiments described in this thesis were performed using ultracold clouds of ^{87}Rb . In this Chapter I describe the techniques and interactions that make our experiments possible. This Chapter is not ~~meant to be~~ an extensive survey of atomic physics but rather covers the topics that are most relevant to my experiments. The references I included are helpful if the reader is interested in learning the details of the derivations or wants to expand on a given topic. I start by describing the electronic structure of ^{87}Rb . Then I review the interactions of atoms with magnetic fields and its application to magnetic trapping. I describe the foundations of atom-light interactions that make possible both laser cooling and trapping of atoms and give rise to Raman induced transitions. Finally I discuss coherent processes that use the magnetic and electric dipole interaction and are relevant to the experiments presented in Chapters 5, 6 and 8. Finally, I discuss resonant absorption imaging which is used to detect atoms after all our experiments are performed.

3.1 Electronic structure of ^{87}Rb

Rb is an Alkali metal (also Li, which exists in our vacuum chamber but was never used). Alkali metals correspond to the first group (leftmost column) of the periodic table and are characterized by having a single valence electron, which makes the description of their internal structure much simpler than that of other elements. We can describe the state of an electron in an atom by its angular momentum $\hat{\mathbf{L}}$ and its spin $\hat{\mathbf{S}}$. Because of Pauli's exclusion principle there can not be two electrons with the same quantum numbers and in multi-electron atoms they tend to fill 'shells' of different angular momentum values, historically labeled by the letters S , P , D , F , ...¹ (corresponding to $L = 1, 2, 3, 4, \dots$). In particular Rb has 4 filled shells and one electron in the $5S$ shell, where the number 5 corresponds to the principal quantum number n . Figure 1 shows the energy levels of the ground state $5S$ and its closest $5P$ orbital.

The atomic level structure is modified by relativistic effects. In particular the relativistic treatment of the electron's motion gives rise to an interaction between the electron's intrinsic magnetic moment (the spin) $\hat{\mathbf{S}}$ and the orbital angular momentum $\hat{\mathbf{L}}$. This spin-orbit coupling interaction $\hat{H}_{\text{fs}} = A_{\text{fs}} \mathbf{L} \cdot \mathbf{S}$ causes the fine structure splitting of the electronic orbitals into levels with different total electronic angular

¹This terms were used to describe the lines in the emission spectra when they were first discovered. S stands for sharp, P for principal D for diffuse and F for further noted

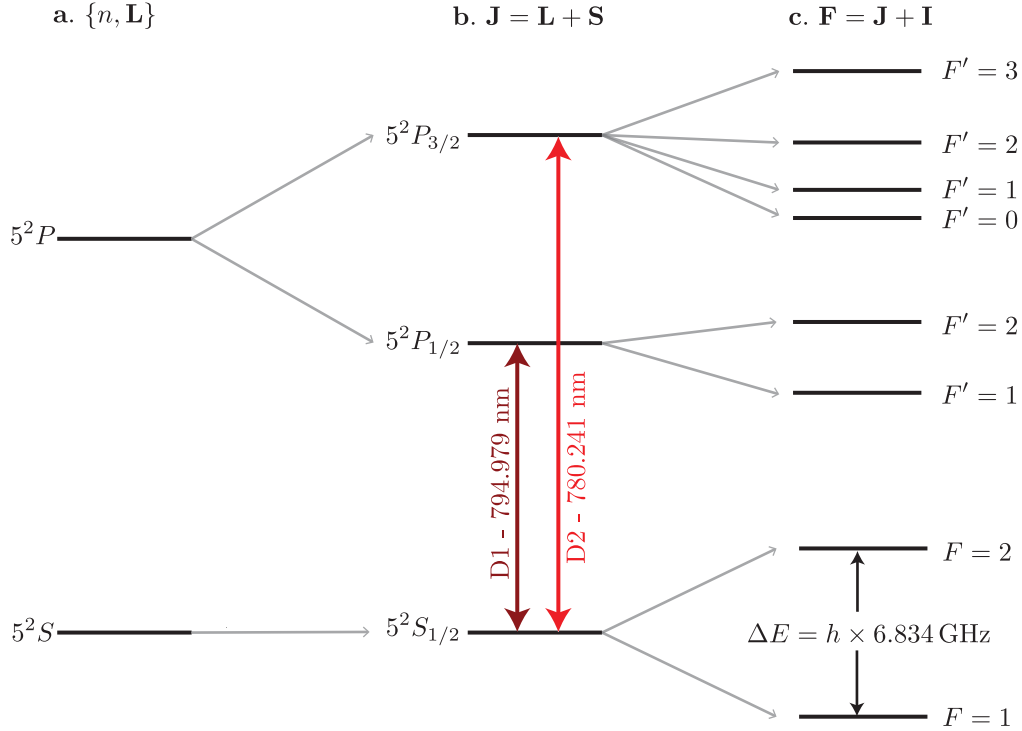


Figure 1: ^{87}Rb level structure (not to scale). **a.** Ground and first excited state electronic configuration of ^{87}Rb given by the $\{n, \mathbf{L}\}$ quantum numbers. **b.** The interaction between the orbital angular momentum and the spin of the electron leads to the fine splitting of orbitals with $L > 0$. The splitting of the 5^2P line gives rise to the D1 and D2 lines. **c.** The interaction between the total angular momentum and the nuclear spin causes the fine structure levels to split further into states characterized by the quantum number F .

momentum $\hat{\mathbf{J}} = \hat{\mathbf{L}} \cdot \hat{\mathbf{S}}$. Figure 1b show the $5^2S_{1/2}$, $5^2P_{1/2}$ and $5^2P_{3/2}$ electronic configurations that arise from this splitting, where the subscript indicates the value of J . For S ($L = 0$) orbitals $J = 1/2$ is the only possible value and the levels are not split. For the P orbital ($L = 1$) J and a single electron with $S = 1/2$, J can be $1/2$ or $3/2$ and the P orbital splits into two levels. The $5^2S_{1/2} \rightarrow 5^2P_{1/2}$ is known as the D1 line and has wavelength $\lambda = 794.979 \text{ nm}$ and $5S_{1/2} \rightarrow 5P_{3/2}$ transition is known as the D2 line and has $\lambda = 780.241 \text{ nm}$ [1].

The atomic level structure gets further modified by the magnetic interaction of the electron with the nuclear spin \mathbf{I} . This is another kind of spin-orbit interaction that gives rise to the hyperfine splitting of the atomic levels which can be described by the Hamiltonian $\hat{H}_{\text{hfs}} = A_{\text{hfs}} \mathbf{I} \cdot \hat{\mathbf{J}}$. A complete derivation of \hat{H}_{hfs} can be found in [2]. The hyperfine levels correspond to different values of the total angular momentum $\hat{\mathbf{F}} = \hat{\mathbf{J}} + \hat{\mathbf{I}}$. For ^{87}Rb $I = 3/2$ [1] which results in the level structure shown in Figure 1c.

3.2 Interaction between atoms and magnetic fields

Atoms have an intrinsic magnetic moment that is given by the sum of nuclear and electronic moments

$$\hat{\mu} = -\frac{\mu_B}{\hbar}(g_S \hat{\mathbf{S}} + g_L \hat{\mathbf{L}} + g_I \hat{\mathbf{I}}) \quad (3.1)$$

where μ_B is the Bohr magneton and g_S , g_L and g_I are the Landé ‘ g -factors’ corresponding to the spin, orbital and nuclear angular momentum. In the presence of an external magnetic field \mathbf{B} , the internal levels of an atom get modified due to the Zeeman [3] interaction

$$\hat{H}_{\text{Zeeman}} = -\hat{\mu} \cdot \mathbf{B}. \quad (3.2)$$

If the energy shift due to the Zeeman interaction is small compared to the hyperfine splitting so that F is a good quantum number we can write

$$\hat{H}_{\text{Zeeman}} = \frac{\mu_B g_F}{\hbar} \hat{\mathbf{F}} \cdot \mathbf{B} \quad (3.3)$$

where the hyperfine Landé g -factor is

$$g_F = g_J \frac{F(F+1) - I(I+1) + J(J+1)}{2F(F+1)} + g_I \frac{F(F+1) + I(I+1) - J(J+1)}{2F(F+1)} \quad (3.4)$$

and

$$g_J \approx 1 + \frac{J(J+1) + S(S+1) - L(L+1)}{2J(J+1)}. \quad (3.5)$$

The total energy shifts can be calculated by diagonalizing the full atomic Hamiltonian including the fine and hyperfine structure terms. Figure 2 shows the energies of the m_F levels in the $F = 1$ and $F = 2$ manifolds of ^{87}Rb as a function of magnetic field. If the magnetic field is small then the Zeeman term can be treated as a perturbation to the atomic Hamiltonian and the energy split is linear with the magnitude of the field $E_{m_F} = g_F \mu_B m_F B$, what is known as the ‘linear Zeeman regime’ where F and m_F are good quantum numbers. In contrast, in the ‘Pachen-Back regime’ at large magnetic fields² the Zeeman term dominates over the fine and hyperfine terms and therefore the good quantum numbers of the system are J and m_J . Our experiments typically operate in an intermediate regime ($B \sim 10 - 30$ G, the gray box in Figure 2) where the energy of $m_F = 0$ gets a small shift in energy that is quadratic in B . For atoms in $F = 1$ we define this quadratic Zeeman shift as $\epsilon = E_0 - (E_{+1} - E_{-1})/2$, where E_{m_F} is the Zeeman shift for state m_F .

For the particular case of $J = 1/2$ (like the ground state of Alkalies) the Zeeman energies can be found analytically using the Breit-Rabi formula [4]

$$E_{m_F} = -\frac{1}{2(2I+1)} + \frac{\mu_B g_I m_F B}{\Delta E_{\text{hf}}} + \frac{1}{2} \sqrt{1 + \frac{4m_F}{2I+1} x + x^2}, \quad (3.6)$$

²A couple orders of magnitude larger than the fields we operate at.

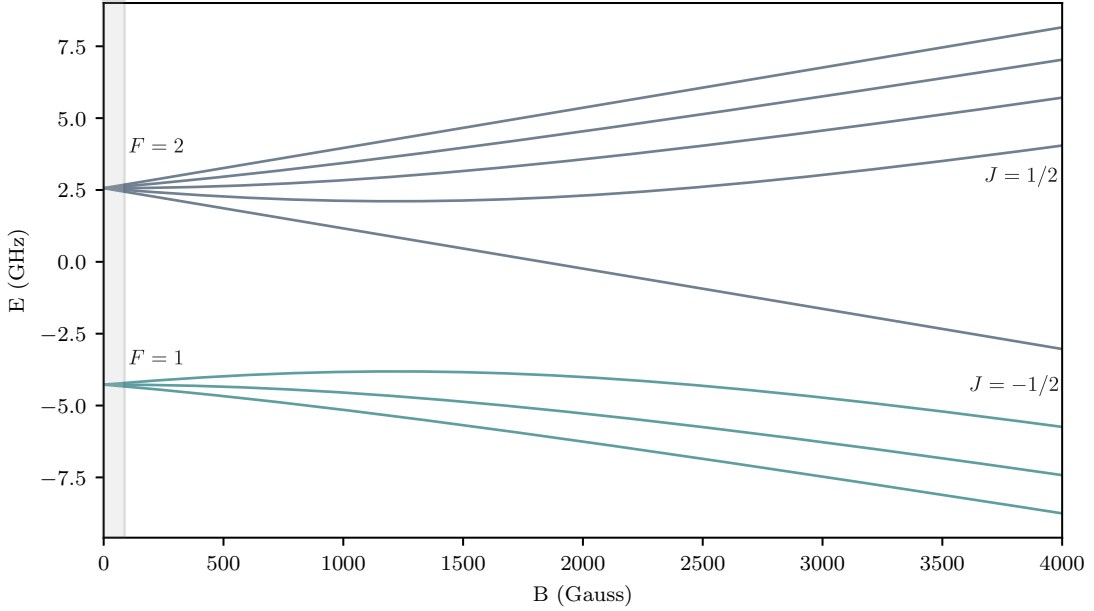


Figure 2: Zeeman splitting of the $5^2S_{1/2}$ manifold of ^{87}Rb . At small magnetic fields F and m_F are good quantum numbers describing the system and at large magnetic fields (Pachen-Back regime) the states are described by the J and m_J . Our experiments operate in the regime marked by the small gray box ($B < 35$ G).

where $\Delta E_{\text{hf}} = A_{\text{hf}}(J + 1/2)$ and $x = (g_J - g_I)\mu_B B_z / \Delta E_{\text{hf}}$. Figure 2 shows the energies of the m_F levels for the $F = 1$ and $F = 2$ manifolds of ^{87}Rb .

3.2.1 Magnetic trapping

The sign of the Zeeman energy for different m_F state can be used to create state dependent traps for atoms. In the lab we implement magnetic traps using quadrupole magnetic fields produced by a pair of anti-Helmholtz coils. The magnetic field near the center of the coils can be written as

$$\mathbf{B} = B'(x\mathbf{e}_x + y\mathbf{e}_y - 2z\mathbf{e}_z) + \mathbf{B}_0 \quad (3.7)$$

where \mathbf{B}_0 is a constant magnetic field, for simplicity I will assume that $\mathbf{B}_0 = B_0\mathbf{e}_z$. The Zeeman Hamiltonian gives a trapping potential

$$\begin{aligned} U(\mathbf{r}) &= g_F \mu_B m_F B' \sqrt{x^2 + y^2 + 4 \left(z - \frac{B_0}{2B'} \right)^2} \\ &\approx g_F \mu_B m_F B' \left(\rho + 2 \left| z - \frac{B_0}{2B'} \right| \right) \end{aligned} \quad (3.8)$$

where $\rho^2 = x^2 + y^2$ and the approximation on the second line is valid for small displacements from the trap center.

The sign of the magnetic moment determines which states can be trapped. For ^{87}Rb the $|F = 1, m_F = -1\rangle$, $|F = 2, m_F = 2, 1\rangle$ are magnetically trappable.



3.3 Interaction between atoms and electric fields

In this section I will discuss the interaction between atoms and electric fields. After laying the foundations I will discuss applications using off-resonant electromagnetic radiation such as optical dipole traps and Raman transitions. I will not cover laser cooling which has been covered extensively in the literature [5, 6] and PhD theses from previous group members [7, 8].

In the presence of an electric field \mathbf{E} an atom can become polarized and therefore its energy levels get modified by the Stark effect [9]. If the electric field is spatially uniform with respect to the atom's size we consider the electric field as a classical object and its effect on the atom can be described by the Hamiltonian [10]

$$\hat{H}_{\text{dip}} = -\hat{\mathbf{d}} \cdot \mathbf{E}, \quad (3.9)$$

where $\hat{\mathbf{d}} = -e \sum_j \hat{r}_j$ is the atomic dipole operator, e is the electron charge and \hat{r}_j are the position operators of the atom's electrons relative to the center of mass of the atom. This approximation, known as the dipole approximation, is valid for electromagnetic radiation when the wavelength is much larger than the size of an atom $\lambda \gg r_{\text{atom}}$ [11].

For a coherent electromagnetic field $\mathbf{E}(\omega, t)$ with angular frequency ω , the dipole Hamiltonian can be written in terms of a dynamic polarizability

$$\hat{H}_{\text{dip}} = -\alpha_{\mu\nu}(\omega) E_\mu^{(+)} E_\nu^{(-)} \quad (3.10)$$

where $\mathbf{E}^{(\pm)}$ are the positive/negative frequency components of the field. $\alpha_{\mu\nu}(\omega)$ can be found by looking at the (time averaged) shift in the energy of a given state using second order time-dependent perturbation theory [11, 12]. For the ground state $|g\rangle$ the polarizability takes the form

$$\alpha_{\mu\nu}(\omega) = \sum_j \frac{2\omega_{jg} \langle g | d_\mu | e_j \rangle \langle e_j | d_\nu | e_j \rangle}{\hbar(\omega_{jg}^2 - \omega^2)}, \quad (3.11)$$

where $|e_j\rangle$ represent the excited states and $\omega_{jg} = (E_j - E_g)/\hbar$. The dipole operator is a rank-2 tensor and can be represented by 3 irreducible tensor operators (see [11] for a complete derivation). In the limit of small magnetic fields so that F and m_F are good quantum numbers describing the state of the atom $|n, F, m_F\rangle$ the dipole

Hamiltonian in this representation takes a convenient form

$$\begin{aligned}\hat{H}_{\text{dip}} = & \alpha^{(0)}(\mathbf{E}^{(-)} \cdot \mathbf{E}^{(+)} + i\alpha^{(1)}(\mathbf{E}^{(-)} \times \mathbf{E}^{(+)})) \cdot \hat{\mathbf{F}} \\ & + \alpha^{(2)} E_i^{(-)} E_j^{(+)} \left(\frac{1}{2}(F_i F_j + F_j F_i) - \frac{1}{3} \hat{\mathbf{F}}^2 \delta_{i,j} \right),\end{aligned}\quad (3.12)$$

where $\alpha^{(0)}$, $\alpha^{(1)}$ and $\alpha^{(2)}$ are the scalar, vector and tensor polarizabilities respectively and $\hat{\mathbf{F}}$ is the total angular momentum operator. For all our experiments $\alpha^{(2)}$ is very small so I will limit the discussion to the effect of the first two terms. The scalar term is responsible for the dipole force that allow us to trap atoms using off-resonant light and the vector component is necessary for engineering spin-orbit coupling and other spin-dependent potentials through two-photon processes.

3.3.1 Scalar polarizability

The scalar polarizability takes the form

$$\alpha^{(0)} = \sum_j \frac{2\omega_{jg} \langle g | \mathbf{d} \cdot \hat{\epsilon} | e_j \rangle|^2}{\hbar(\omega_{jg}^2 - \omega^2)}, \quad (3.13)$$

where $\hat{\epsilon}$ represents the polarization vector of the light. The matrix element can be expressed in terms of the Clebsch-Gordan coefficients and the reduced matrix element using the Wigner-Eckart theorem [13]. For the ground state of an Alkali atom ($J = 1/2$) and if the detuning is large compared to the hyperfine splitting the expression above gets simplified to

$$\alpha^{(0)} \approx \sum_{J'} \frac{2\omega_{JJ'} |\langle J = 1/2 | \mathbf{d} | J' \rangle|^2}{3\hbar(\omega_{JJ'}^2 - \omega^2)}. \quad (3.14)$$

The dipole matrix elements needed to compute the polarizability are related to the transition scattering rate via Fermi's golden rule [11, 13]

$$\Gamma_{JJ'} = \frac{\omega_{JJ'}^2}{3\pi\epsilon_0\hbar c^3} \frac{2J+1}{2J'+1} |\langle J | \mathbf{d} | J' \rangle|^2, \quad (3.15)$$

and combining this with the expression for the intensity of the electric field $I(\mathbf{r}) = 2\epsilon_0 c |\mathbf{E}(\mathbf{r})|^2$ it can be shown that for linearly polarized light the energy of the ground state manifold is shifted by

$$U(\omega, \mathbf{r}) = -\frac{\pi c^2 I(\mathbf{r})}{2} \left[\frac{\Gamma_{D1}}{\omega_{D1}^3} \left(\frac{1}{\omega + \omega_{D1}} - \frac{1}{\omega - \omega_{D1}} \right) + \frac{2\Gamma_{D2}}{\omega_{D2}^3} \left(\frac{1}{\omega + \omega_{D2}} - \frac{1}{\omega - \omega_{D2}} \right) \right], \quad (3.16)$$

where only the the most significant contribution from the closest transitions (the D1 and D2 lines) are included. Here $U(\mathbf{r})$ is related to the real part of the polarizability which is in fact a complex valued number. So far I have only considered a real valued polarizability by assuming the excited states have an infinitely long lifetime.

However, in reality the atom can spontaneously emit photons and decay. This exponential decay can be accounted for by adding an imaginary contribution to the energies $\omega_D \rightarrow \omega_D + i\Gamma_D \omega^3/\omega_D^3$ of the D1 and D2 transitions [14]. The scattering rate is related to the imaginary part of the polarizability and is given by

$$\Gamma(\omega, \mathbf{r}) = \frac{\pi c^2 I(\mathbf{r})}{2\hbar} \left[\frac{\Gamma_{D1}\omega^3}{\omega_{D1}^6} \left(\frac{1}{\omega + \omega_{D1}} - \frac{1}{\omega - \omega_{D1}} \right)^2 + \frac{2\Gamma_{D2}\omega^3}{\omega_{D2}^6} \left(\frac{1}{\omega + \omega_{D2}} - \frac{1}{\omega - \omega_{D2}} \right)^2 \right] \quad (3.17)$$

The energy shift $U(\omega, \mathbf{r})$ is a conservative term and is related to dipole trapping while the scattering term $\Gamma(\omega, \mathbf{r})$ is dissipative and is important for laser cooling. In the context of engineering potentials for ultracold atoms with off-resonant light, the scattering is translated into heating because every time an atom emits a photon with angular frequency ω_L it gets a recoil momentum $\hbar\mathbf{k}_L$. If the frequency ω satisfies the relation $\omega + \omega_D \gg \omega - \omega_D$, as is often the case, we can neglect the terms proportional to $1/(\omega + \omega_D)$, an approximation typically known as the rotating wave approximation (RWA). If the RWA is valid then the frequency dependence of both the energy shifts and the scattering rates will be given by the detuning from the D1 and D2 transitions.

3.3.1.1 Optical trapping

One important application of the scalar light-shift is to create optical traps for clouds of ultracold atoms. An optical field with non-uniform spatial intensity generates traps (and anti-traps) for the atoms which experience a force proportional to the intensity gradient $F_{\text{dip}} = -\nabla U(\mathbf{r})$. The attractive or repulsive nature of the trap depends on the sign of $U(\mathbf{r})$ which is determined by the sign of the detuning (blue-detuned traps are repulsive and red-detuned traps are attractive)[TODO: make nice figure of dipole trap if I have time]. The production of BECs in our lab relies on the use of focused Gaussian laser beams with $\lambda = 1064$ nm. The intensity profile of a focused Gaussian beam propagating along \mathbf{e}_z is given by

$$I(x, y, z) = \frac{2P}{\pi\omega^2(z)} e^{-\frac{x^2+y^2}{\omega^2(z)}} \quad (3.18)$$

where P is the total power of the beam and the $1/e^2$ radius is given by $w(z) = w_0 \sqrt{1 + z^2/z_R^2}$ where the minimum radius w_0 is known as the waist and $z_R = \pi\omega_0^2/\lambda$ is the Rayleigh range. If the extent of an atomic cloud is small compared to the size of the beam we can perform a Taylor expansion around $\mathbf{r} = 0$ to obtain the trapping potential

$$U(\mathbf{r}) = -U_0 \left(1 - 2 \frac{x^2 + y^2}{\omega_0^2} - \frac{z^2}{z_R^2} \right). \quad (3.19)$$

The oscillation frequencies of the trap along the radial direction are $\omega_r = (4U_0/m\omega_0^2)^{1/2}$ and along the axial direction $\omega_z = (2U_0/mz_R)^{1/2}$. The beam waist is usually much smaller than the Rayleigh range ($\omega_0 \sim 50 - 150$ nm for my experiments) and therefore the trap is much stronger along the axial direction. To get around this we use

a ‘crossed dipole trap’ which is formed by a combination of two cross-polarized³ focused Gaussian beams propagating along perpendicular axes, ensuring that we get good confinement of atoms along all spatial directions.

3.3.2 Vector polarizability and effective magnetic fields

For Alkali atoms the vector polarizability takes the form [11, 15]

$$\alpha^{(1)} = \frac{2\alpha^{(0)}\Delta_{fs}}{3(\tilde{E} - \hbar\omega)} \quad (3.20)$$

where $\Delta_{fs} = 3A_{fs}/2$ and $\tilde{E} = (2E_{D_1} + E_{D_2})$. If we recall the Zeeman Hamiltonian introduced in Section 3.2, the term proportional to the vector polarizability in Equation 3.12 looks very similar to Equation 3.2 for an effective magnetic field

$$\mathbf{B}_{\text{eff}} = -\frac{i\hbar}{\mu_B g_J} \alpha^{(1)} (\mathbf{E}^* \times \mathbf{E}). \quad (3.21)$$

For the intensities that we typically operate at, the vector light shift is small and can be treated as a perturbation. The Hamiltonian resulting from this effective magnetic field can be written as

$$\hat{H}_{\text{eff}} = \frac{\mu_B g_F}{\hbar} \mathbf{B}_{\text{eff}} \cdot \hat{\mathbf{F}} \quad (3.22)$$

3.3.2.1 Raman coupling

The vector light shift enables the realization of various spin dependent potentials in the lab. In the experiments presented in Chapters 5 and 8 I used combinations of cross polarized laser beams such that the total electric field $\mathbf{E}^* \times \mathbf{E} \neq 0$ and we induced two-photon Raman transitions. A Raman transition is a two-photon process between two ground states that uses an intermediate state that is off-resonantly coupled as is shown in Figure 3a. Due to the large detuning, the population transferred into the intermediate state is negligible and the state can be adiabatically eliminated [16]. In our experiments we typically couple the m_F levels of the $F = 1$ manifold after applying a bias magnetic field such that ϵ is non-negligible.

Consider two laser beams counter propagating along \mathbf{e}_x and with polarizations along \mathbf{e}_y and \mathbf{e}_z as is shown in Figure 3b. The electric field from the Raman beams is given by

$$\mathbf{E}(x, t) = E_a \cos(k_a x - \omega_a t) \mathbf{e}_y + E_b \cos(k_b x + \omega_b t) \mathbf{e}_z, \quad (3.23)$$

and consequently

$$\mathbf{E}^* \times \mathbf{E} = 2iE_a E_b \cos(2k_L x - \omega_{a,b} t) \mathbf{e}_x, \quad (3.24)$$

³The beams are cross-polarized to avoid interference between them

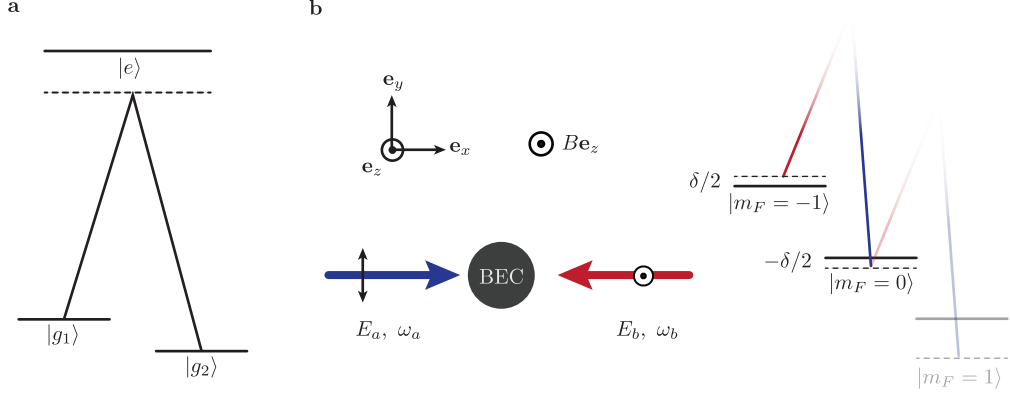


Figure 3: **a.** A Raman transition is a two photon process that couples two ground state through and intermediate far detuned state. **b.** We induce Raman transitions using a pair of cross-polarized laser beams whose and we set the difference in their angular frequencies close to the Zeeman splitting between two consecutive m_F states.

where $\omega_{a,b} = \omega_a - \omega_b$. The Raman Hamiltonian is given by

$$\hat{H}_R = \Omega \cos(2k_L x - \omega_{a,b} t) \hat{F}_x \quad (3.25)$$

where $\Omega = \alpha^{(1)} g_F E_a E_b / g_J \propto \sqrt{I_a I_b}$ is the Raman coupling strength. The geometry and wavelength of the Raman fields determine the natural units of the system: the single photon recoil momentum $k_L = 2\pi/\lambda_R$ and its associated recoil energy $E_L = \hbar^2 k_L^2 / 2m$, as well as the direction of the recoil momentum $\mathbf{k}_L = k_L \mathbf{e}_x$. For most experiments we tune to what is known as the ‘magic wavelength’ or tune-out wavelength [17] $\lambda_R = 790.034$ nm, at which the ground-state scalar polarizability vanishes and the scattering rate is reduced (Figure 4a,c). We occasionally had to tune away from the magic wavelength, for example when we were starving for laser power and wanted to increase our Raman coupling strength; Figure 4b shows the dependence of the Raman coupling strength on wavelength and 4d shows the decay in number of Raman dressed atoms as a function of time for different wavelengths.

In a frame rotating with angular frequency $\omega_{a,b}$ corresponding to applying the unitary transformation $\hat{U}(t) = \exp(-i\omega_{a,b} t \hat{F}_z)$ and neglecting the fast terms rotating at frequency $2\omega_{a,b}$ (applying a RWA) the transformed Hamiltonian is

$$\hat{U}^\dagger \hat{H}_R \hat{U} - i\hbar \hat{U}^\dagger \partial_t \hat{U} = \omega_{a,b} \hat{F}_z + \frac{\Omega}{2} \cos(2k_L x) \hat{F}_x - \frac{\Omega}{2} \sin(2k_L x) \hat{F}_y, \quad (3.26)$$

which describes a helically precessing magnetic field with period $\lambda_R/2$.

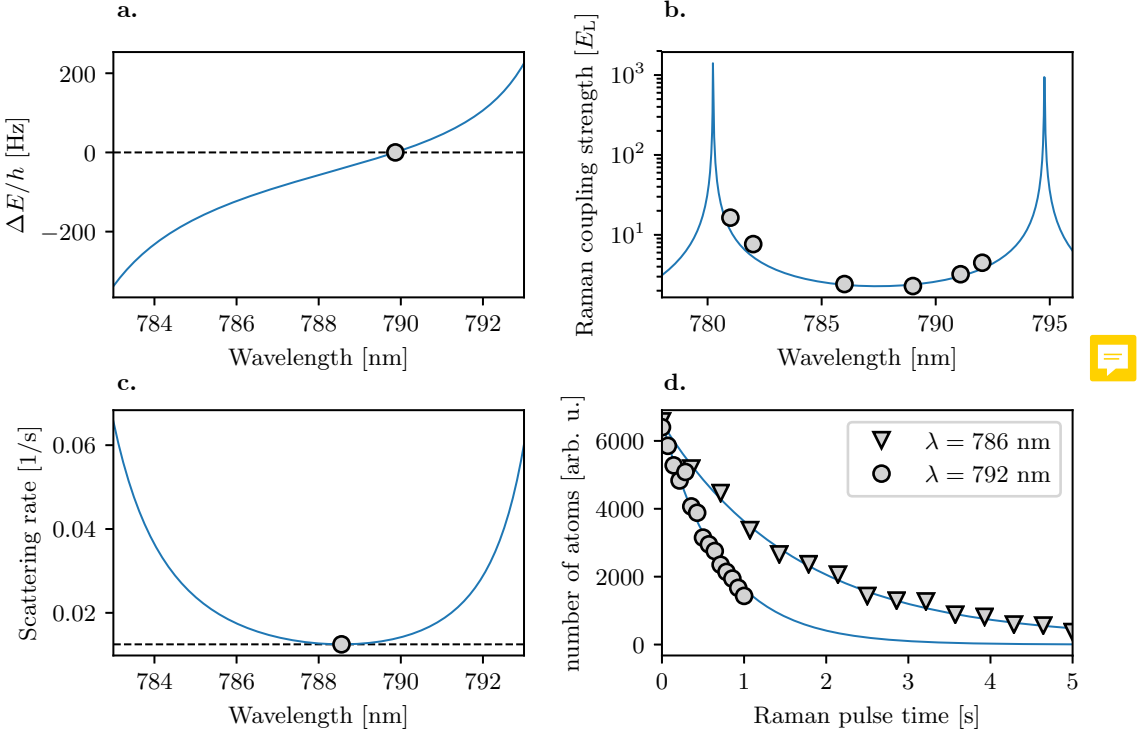


Figure 4: **a.** Scalar polarizability as a function of wavelength near the D1 and D2 lines of ^{87}Rb . We typically tune our Raman laser beams near the magic wavelength $\lambda = 790.034 \text{ nm}$. **b.** Raman coupling strength as a function of wavelength measured for a pair of Raman beams with waist $w_0 \sim 150 \mu\text{m}$ and powers of $50, 10 \mu\text{W}$. **c.** Scattering rate as a function of wavelength, while it is not minimized at 790 nm its value is kept relatively low. **d.** Decay in number of Raman dressed atoms as a function of hold time for the same beam parameters as in **b.**. At $\lambda = 786 \text{ nm}$ the $1/e$ lifetime is $\tau = 1.64 \text{ s}$ and for $\lambda = 792 \text{ nm}$ it is reduced to $\tau = 0.72 \text{ s}$.

3.3.2.2 Spin-orbit coupling

The Raman Hamiltonian from Equation 3.26 can be massaged a bit more to make it look like a spin-orbit coupled (SOC)⁴ Hamiltonian that is familiar to condensed matter physicists. If we apply a spin-dependent momentum boost which is described by the unitary operator $\hat{U}(k_{\text{L}}) = \exp(i2k_{\text{L}}x\hat{F}_z)$ the full Hamiltonian including the Raman coupling and the free particle energies is transformed to

$$\hat{H}_{\text{SOC}} = \frac{\hbar^2}{2m} (\hat{q}_x - 2k_{\text{L}}\hat{F}_z)^2 + \frac{\Omega}{2}\hat{F}_x + \delta\hat{F}_z + \hbar\epsilon \left(\mathbb{1} - \frac{\hat{F}_z^2}{\hbar^2} \right), \quad (3.27)$$

⁴Not to be confused with the spin-orbit coupling giving rise to the fine and hyperfine structure mentioned earlier, perhaps a better name could be spin-momentum coupling

where $\delta = E_{-1} - \omega_{a,b}$. We can go from a 3 level system to an effective spin-1/2 system if we set $\Delta\omega = E_{-1} - E_0$ and consider a sizable quadratic Zeeman shift ϵ , the $m_F = 1$ state can be adiabatically eliminated [18] and the Hamiltonian becomes

$$\hat{H}_{SOC} = \frac{\hbar^2}{2m}(q_x - k_L \hat{\sigma}_y)^2 + \frac{\hbar}{2}\Omega \hat{\sigma}_z + \frac{\hbar}{2}\delta \hat{\sigma}_y \quad (3.28)$$

where $\sigma_{x,y,z}$ are the Pauli matrices. The Hamiltonian above corresponds to an equal superposition of Rashba-type [19] ($\propto \hat{\sigma}_x k_y - \hat{\sigma}_y k_x$) and Dresselhaus-type [20] ($\propto -\sigma_x k_y - \sigma_y k_x$) SOC with an effective magnetic field $\propto \Omega$ in the $\mathbf{e}_y - \mathbf{e}_z$ plane [18, 21]. In Chapter 8 I discuss the Rashba term in more detail and introduce a way of engineering a system with only Rashba-type SOC using multiple internal levels and Raman transitions.

3.4 Coherent manipulation

 In this section I describe quantum coherent processes that are driven using the magnetic and electric dipole interactions described in previous sections. We rely on this techniques both for state preparation and characterization of our system. In all of the cases I consider a system described by the Hamiltonian

$$\hat{H} = \hat{H}_0 + \hat{H}_I(t) \quad (3.29)$$

where \hat{H}_0 describes unperturbed atomic levels and $\hat{H}_I(t)$ is a time dependent interaction. For simplicity I consider only a two-level system

$$\hat{H}_0 = \hbar \begin{pmatrix} \omega_g & 0 \\ 0 & \omega_e \end{pmatrix} \quad (3.30)$$

where with $|g\rangle$ and $|e\rangle$ are the unperturbed ground and excited states with energy $\hbar\omega_i$ are the energies of the unperturbed states.

3.4.1 Rabi oscillations

First I consider an interaction term that oscillates with frequency ω close to the transition energy $\omega_{ge} = \omega_g - \omega_e$

$$\hat{H}_I = \hbar \begin{pmatrix} 0 & \Omega \cos(\omega t) \\ \Omega^* \cos(\omega t) & 0 \end{pmatrix} \quad (3.31)$$

the coupling strength Ω here could be related to an electric dipole transition $\Omega \propto \langle g | \mathbf{d} \cdot \mathbf{E} | e \rangle$ ⁵ or magnetic dipole $\Omega \propto \langle g | \boldsymbol{\mu} \cdot \mathbf{B} | e \rangle$ transition matrix element. The

⁵For our system intensities $\Gamma \gg \Omega$ and we don't observe Rabi oscillations from (single photon) electric dipole transitions.

state of the system at any given time is given by

$$|\Psi\rangle = c_g(t)e^{-i\omega_g t} |g\rangle + c_e(t)e^{-i\omega_e t} |e\rangle, \quad (3.32)$$

and substituting this expression into the time dependent Schrödinger equation we find that

$$\begin{aligned}\dot{c}_g(t) &= \frac{\Omega}{2} (e^{i(\omega-\omega_{ge})t} + e^{-i(\omega+\omega_{ge})t}) c_e \\ \dot{c}_e(t) &= \frac{\Omega^*}{2} (e^{i(\omega-\omega_{ge})t} + e^{-i(\omega+\omega_{ge})t}) c_g.\end{aligned}\quad (3.33)$$

We can apply a RWA if the term $\omega + \omega_{ge}$ is large compared to $\omega - \omega_{ge}$. The resulting coupled differential equations can be solved in a standard way by differentiating \dot{c}_e one more time and substituting \dot{c}_g . If we assume that at $t = 0$ the system is prepared in $|g\rangle$ the population in $|e\rangle$ describes what is known as a Rabi oscillation [22]

$$|c_e(t)|^2 = \frac{\Omega^2}{\Omega^2 + \delta^2} \sin^2 \left(\frac{\sqrt{\Omega^2 + \delta^2}}{2} t \right) \quad (3.34)$$

where $\delta = \omega - \omega_{ge}$ is a detuning and $\tilde{\Omega} = \sqrt{\Omega^2 + \delta^2}$ is known as the generalized Rabi frequency. The Hamiltonian after applying the RWA can be written as

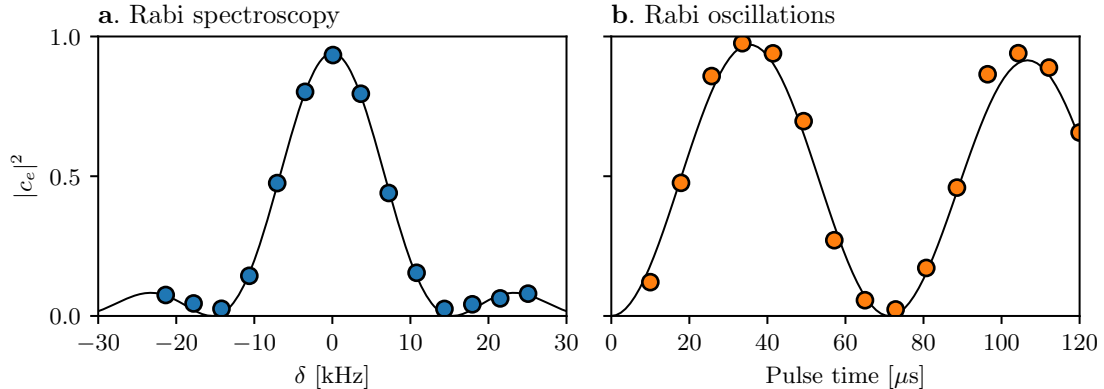


Figure 5: The Rabi cycle. **a.** Population transferred to the excited state as a function of detuning for a $60 \mu s$ pulse and $\Omega = 7.1 \text{ kHz}$. **b.** Population transferred as a function of time for a $\Omega = 14 \text{ kHz}$ close to resonance.



$$\hat{H}_0 = \hbar \begin{pmatrix} -\delta/2 & \Omega/2 \\ \Omega^*/2 & \delta/2 \end{pmatrix}, \quad (3.35)$$

and its eigenenergies correspond to $E_{\pm} = \pm \tilde{\Omega}/2$. Notice that the difference between the eigenenergies $E_+ - E_-$ is exactly equal to the frequency at which the populations

in $|g, e\rangle$ oscillate, this will come up again in Chapter 5. Figure 5a shows the population in $|e\rangle$ as a function of δ for a π pulse ($\delta = 0, \Omega t = \pi$). The location of the peak in this curve is as a way to find the transition frequency (we use this method in Chapter 6). Figure 5b shows the population transferred into $m_F = 0$ from $m_F = -1$ as a function of time; we typically look at the frequency of these Rabi oscillations to calibrate the coupling strength of an effective two-level system.

3.4.2 Ramsey interferometer

Now I consider a Ramsey interferometer [23], a setup that is relevant to Chapters 6 and 8. The interaction Hamiltonian is the same as in the previous section but rather than being on continuously it is pulsed on for a time $\tau = \pi/2\Omega$ (a $\pi/2$ pulse), then the system is let to evolve only under \hat{H}_0 for a variable time t_{dark} and finally a second $\pi/2$ pulse is applied. Figure 6a illustrates this protocol: the $\pi/2$ pulses can be thought of as $\pi/2$ rotations on the Bloch sphere along \mathbf{e}_x transforming the initial state $|g\rangle \rightarrow (|g\rangle + |e\rangle)/\sqrt{2}$. During the dark time the system precesses on the equator of the Bloch sphere by an angle δt_{dark} and finally the second pulse rotates the state along the \mathbf{e}_x axis again. The probability of measuring the excited state is related to the phase accumulated during the dark time is given by

$$|c_e(2\tau + t_{\text{dark}})|^2 = \left| \frac{\Omega\tau}{2} \left[\frac{\sin(\delta\tau/2)}{\delta\tau/2} \right]^2 \cos^2 \left(\frac{\delta t_{\text{dark}}}{2} \right) \right|, \quad (3.36)$$

where the oscillation frequency is only determined by the detuning. In contrast, for a Rabi oscillation the detuning adds in quadrature with Ω , which suppresses the effect of the detuning when it is large as $\tilde{\Omega} \approx \Omega + \delta^2/2\Omega$. This will be important in Chapter 6 and additionally in Chapter 8 I rely on a variation of the Ramsey interferometer to perform quantum state tomography. Figure 6b shows an example of a Ramsey fringe as a function of detuning δ that we measured using two states coupled with $\Omega = 1$ kHz.

3.4.3 Floquet theory

The RWA has been used multiple times throughout this Chapter so that the Hamiltonian describing a driven systems can effectively be viewed as time independent. This approximation is valid most of the time for our experiments, however, if we want to give a complete description of a time periodic system Floquet theory can be helpful. I will give a brief overview of Floquet theory using a matrix approach that is particularly useful for numerical computations.

Consider a time periodic Hamiltonian $\hat{H}(t) = \hat{H}(t+T)$. We can write in terms of its Fourier components

$$\hat{H}(t) = \sum_{j=-\infty}^{\infty} \exp[ij\omega t] \hat{H}_j, \quad (3.37)$$

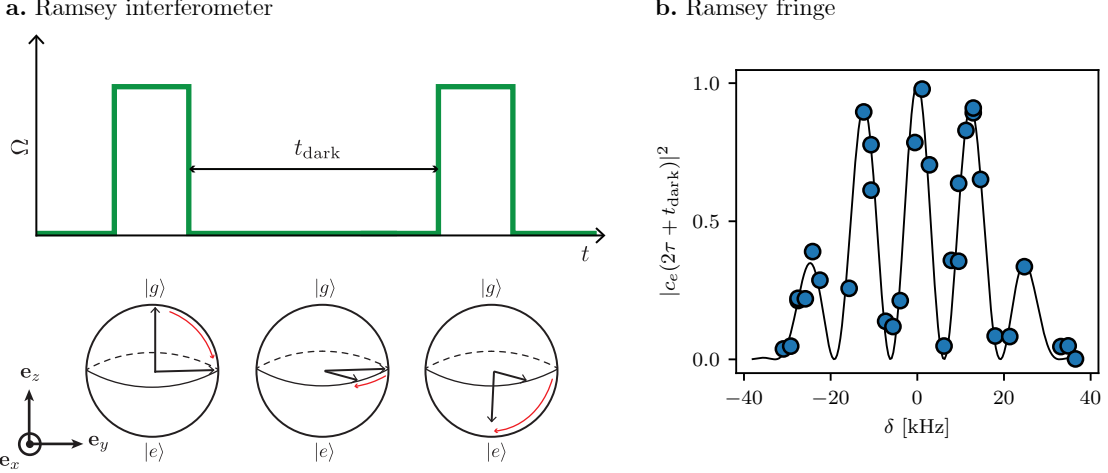


Figure 6: **a.** A Ramsey interferometer: Two $\pi/2$ pulses are separated by a time t_{dark} . The phase accumulated in the interferometer is equal to the detuning multiplied by the dark time. **b.** A Ramsey interference fringe obtained from coupling two levels using an RF field with $\Omega = 1 \text{ kHz}$. We applied a pair of $\tau = 25 \mu\text{s}$ pulses separated by a $50 \mu\text{s}$ wait and varied the detuning by changing the bias magnetic field.

where $\omega = 2\pi/T$ and because \hat{H} is Hermitian the operators must satisfy $\hat{H}_j = \hat{H}_{-j}^\dagger$. The eigenstates of the Hamiltonian can be written in terms of quasi periodic functions⁶

$$|\psi_\epsilon(t)\rangle = \exp(-i\epsilon t/\hbar) \sum_{k=-\infty}^{\infty} \exp[-ik\omega t] |\psi_{\epsilon,k}\rangle \quad (3.38)$$

where the term ϵ is known as the quasi-energy. Inserting this expression into the time-dependent Schrödinger equation gives

$$\sum_k (\epsilon + \hbar\omega k) \exp[-k\omega t] |\psi_{\epsilon,k}\rangle = \sum_{j,j'} \exp[i(j-j')\omega t] \hat{H}_{j'} |\psi_{\epsilon,j}\rangle. \quad (3.39)$$

In order for the equality to be true we must have $j' - j = -k$ because the complex exponentials form an orthonormal basis and we can write

$$\epsilon |\psi_{\epsilon,k}\rangle = \sum_j \left(\hat{H}_{j-l} - \hbar\omega k \delta_{j,k} \times \hat{\mathbb{1}} \right), \quad (3.40)$$

⁶Very much like Bloch wave functions

where $\hat{\mathbb{1}}$ is the identity matrix. The expression can be recast into a matrix form

$$\epsilon \begin{pmatrix} \cdots \\ |\psi_{\epsilon,-1}\rangle \\ |\psi_{\epsilon,0}\rangle \\ |\psi_{\epsilon,1}\rangle \\ \cdots \end{pmatrix} = \begin{pmatrix} \hat{H}_0 + 2\hbar\omega & \hat{H}_1 & \hat{H}_2 & \cdots & \cdots & \cdots \\ \hat{H}_{-1} & \hat{H}_0 + \hbar\omega & \hat{H}_1 & \hat{H}_2 & \cdots & \cdots \\ \hat{H}_{-2} & \hat{H}_{-1} & \hat{H}_0 & \hat{H}_1 & \cdots & \cdots \\ \cdots & \hat{H}_{-2} & \hat{H}_{-1} & \hat{H}_0 - \hbar\omega & \hat{H}_1 & \cdots \\ \cdots & \cdots & \hat{H}_{-2} & \hat{H}_{-1} & \hat{H}_0 - 2\hbar\omega & \cdots \\ \cdot & & & & & \end{pmatrix} \quad (3.41)$$

The quasienergies ϵ can be computed by truncating and then diagonalizing the matrix, and they are grouped into repeating manifolds separated in energy by $\hbar\omega$. The quasienergies within a manifold can be interpreted as the eigenenergies of an effective time-independent Hamiltonian \hat{H}_{Fl} that describes the evolution of the system sampled stroboscopically at an integer number of driving periods, with the time evolution operator $\hat{U}(t_0, t_0 + T) = e^{-iT\hat{H}_{Fl}}$.

Floquet theory played an important role in the engineering of different dispersion relations for atoms in Chapters 5 and 8. I will give an example based on [24], where we considered a pair of Raman beams driving transitions between the m_F states with two different frequencies $\omega_{-1,0}$ and $\omega_{0,+1}$ set to the $m_F = -1 \rightarrow m_F = 0$ and $m_F = 0 \rightarrow m_F = 1$ transitions. By performing independent RWAs with respect to each of these transitions we found that the system could be described by a magnetic Hamiltonian

$$\hat{H} = \frac{\hbar k^2}{2m} + \boldsymbol{\Omega}(x) \cdot \hat{\mathbf{F}} + \Omega_2 \hat{F}_{zz}^{(2)} \quad (3.42)$$

with $\boldsymbol{\Omega}_1(x)/\Omega_1 = \cos(2k_R x)\mathbf{e}_x - \sin(2k_R x)\mathbf{e}_y$, $\hat{F}_{zz}^{(2)}\hbar = \hat{F}_z^2/\hbar^2 - 2/3$ is an element of the quadrupole tensor and $\Omega_2 = (\omega_{-1,0} - \omega_{0,1})/2$ can be interpreted as an effective quadratic Zeeman shift. The competing contributions between kinetic and magnetic ordering energies gave rise to different magnetic phases. Figure 7a. shows the ground branch of the dispersion relation for small $\Omega_1 < 4E_L$ (top) and large $\Omega_1 > 4E_L$ (bottom). As the value of Ω_2 is decreased the magnetization in the system changes as the location of the global minima in the dispersion changes. The experimental parameters Ω_1 and Ω_2 spanned a two-dimensional phase diagram shown in Figure 3.42b that we experimentally mapped. The eigenenergies of Equation 7 are plotted in Figure 7c. However in order to get a good agreement between the experiment and the phase diagram we had use the full Floquet Hamiltonian which results in having modified parameters in Equation 3.42 $\Omega_2^{(\text{eff})} = \Omega_2 + \mathcal{O}(\Omega_1^2/\epsilon)$ (red dotted line in Figure 7b). Figure 7d shows three manifolds of Floquet quasienergies for this system, illustrating their periodic nature.

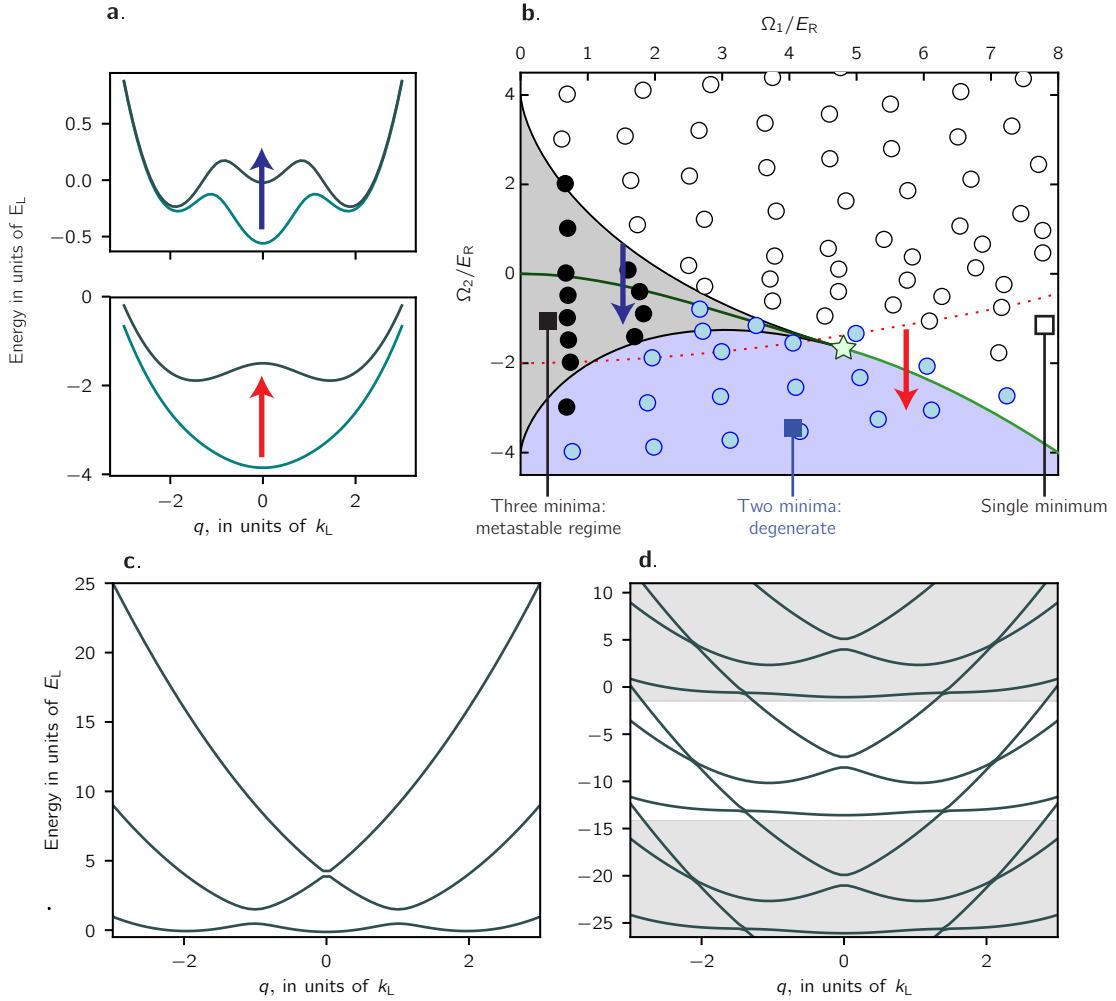


Figure 7: Magnetic phases of a spin-1 SOC system. **a.** Ground state energies of a spin-1 SOC system for $\Omega_1 = 1.5 E_L$ (top) and $\Omega_2 = 1.5 E_L$ (bottom). By changing Ω_2 we moved the location of the central minima. **b.** Phase diagram of a spin-1 SOC system. They green line corresponds to a line of phase transitions where the system goes from magnetized to unmagnetized. **c.** Dispersion relation computed for $\Omega_1 = 2 E_L$, $\Omega_2 = 0$. **d.** Floquet quasienergy dispersion relation for the same parameters. The magnitude of Ω_1 effectively modifies Ω_2 in the RWA Hamiltonian.

3.5 Detection: Resonant absorption imaging

Ultracold atom experiments rely on optical imaging as the main method to probe and characterize the system. In our lab we use resonant absorption imaging which uses a resonant probing laser that is shone at the atomic cloud and then imaged into a charged-coupled device (CCD) camera. From the absorption of the light we can then infer properties about the atoms such as number of atoms, temperature, integrated column density and momentum distribution if we allow the clouds

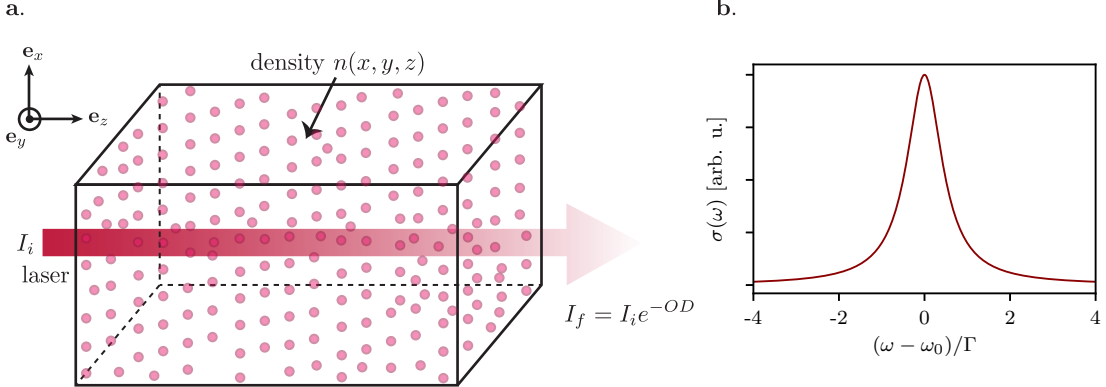


Figure 8: **a.** A laser beam traveling along \mathbf{e}_z through a medium with density $n(x, y, z)$. The intensity decays exponentially with the integrated column density and the scattering cross section $\sigma\omega$. **b.** The scattering cross section has a Lorentzian line shape with a full width half maximum equal to Γ . [TODO: add real data on panel b if I have time.]

to expand.

Consider a laser beam with intensity $I(x, y, z)$ and angular frequency ω propagating along \mathbf{e}_z through a cloud of atoms with density $n(x, y, z)$ as is shown in Figure 8a. We define a (frequency dependent) scattering cross section $\sigma(\omega)$ which characterized the probability of an atom absorbing a probe photon and is given by the Lorentzian function

$$\sigma(\omega) = 3A_{eg} \frac{\pi^2 c^2}{\omega_0^2} \frac{1}{2\pi} \frac{\Gamma}{\delta^2 + \Gamma^2/4} \quad (3.43)$$

plotted in Figure 8b, where Γ is the scattering rate, ω_0 is the transition frequency, $\delta = \omega - \omega_0$ is the detuning and A_{eg} is the Einstein coefficient associated to spontaneous emission. As the beam travels through the cloud it will be absorbed and its intensity is reduced at a rate given by

$$\frac{dI}{dz}(x, y, z) = -n(x, y, z)\sigma(\omega)I(x, y, z). \quad (3.44)$$

In the limit of small intensities we can integrate this expression over the thickness of the cloud and find that the intensity decays exponentially with the density and the scattering cross section

$$I(x, y, z) = I(x, y, 0)e^{-\int_0^z n(x, y, z')\sigma(\omega)dz'}, \quad (3.45)$$

where $OD = \int_0^z n(x, y, z')\sigma(\omega)dz'$ is the optical depth (OD) of the medium. If

we measure the OD of the cloud it is then straightforward to obtain the integrated column density $n(x, y)$. This result, known as the Beer-Lambert law, works well when using low intensity beams.

In the experiment we measure the optical depth of a cloud by imaging the probe into a CCD camera under two different conditions: first in the presence of atoms to measure the attenuated intensity $I_f = I(x, y, z)$ and then without any atoms to get a measure of the initial intensity $I_i = I(x, y, 0)$. The optical depth can then be computed as

$$OD = \ln \left(\frac{I_f}{I_i} \right). \quad (3.46)$$

Figure 9 show the different images used to compute the OD. In practice we take a third image of the background intensity I_{bg} and subtract it from the other two images.

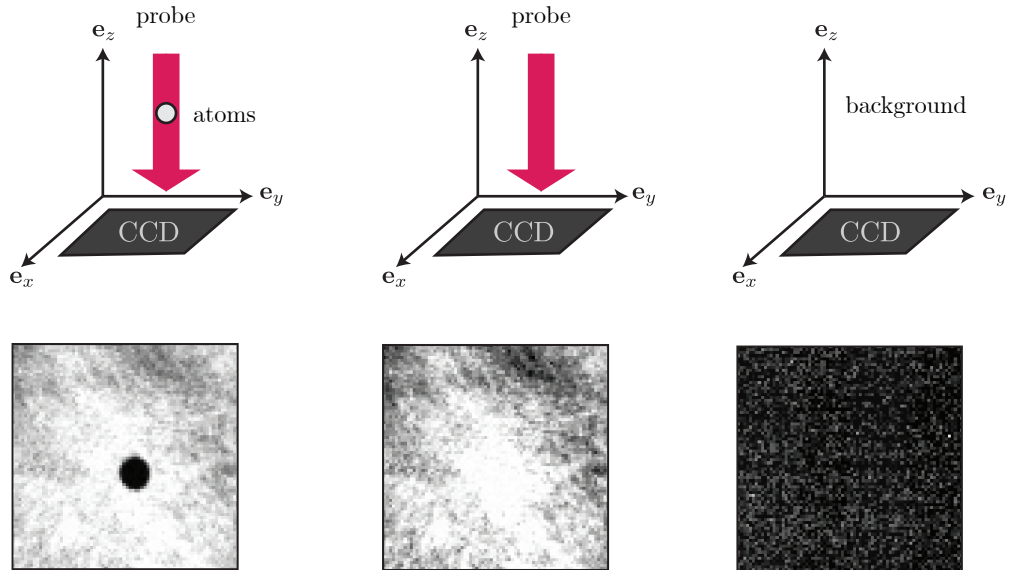


Figure 9: Resonant absorption imaging. An atomic sample is illuminated with a resonant probe whose intensity is later recorded on a CCD camera. Two additional images of the unabsorbed probe intensity and the background intensity are captured in order to reconstruct the optical density of the atoms.

3.5.1 High intensity absorption imaging

The use of the OD to infer the atomic density works well if we assume that the intensity of the probing laser is low such that the atoms mostly stay in the ground state. However at high intensities a significant fraction of the atoms can become excited and effects such as stimulated emission of light have to be taken into account. As a result of this the scattering cross section gets an additional

dependence on intensity (see [25] for a complete derivation)

$$\sigma(\omega, I) = \sigma(\omega) \frac{1}{1 + I/I_{\text{sat}}}, \quad (3.47)$$

where $I_{\text{sat}} = \pi h c \Gamma / 3 \lambda_0^3$ is the saturation intensity, and when $I = I_{\text{sat}}$ the population in the ground and excited state are equal. Integrating Equation 3.44 using the modified expression for $\sigma(\omega, I)$ gives

$$n(x, y) \sigma(\omega) = -\alpha^* \ln(I_f/I_i) + \frac{I_i - I_f}{I_{\text{sat}}}, \quad (3.48)$$

where I have also added an additional dimensionless parameter α^* which can account for imperfections in the imaging process (see [26]).

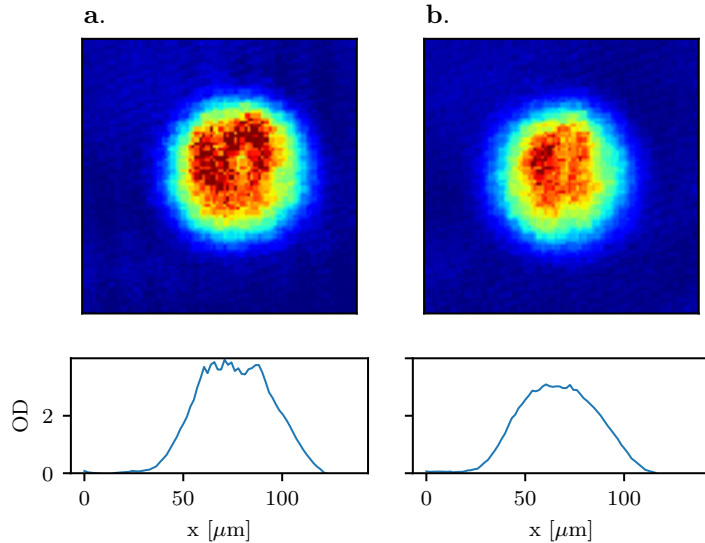


Figure 10: **a.** A BEC imaged at low intensity shows a ‘flat-top’ density profile. **b.** In order to recover the Thomas-Fermi profile it is necessary to image high density BECs with intensities larger than I_{sat} . [TODO: I should try to find better images, this ones don’t look great...]

It is hard reliably measure atomic clouds at low intensity when the OD is of the order of 3 or 4 (such as our BECs) and a significant fraction of the imaging light is absorbed. Due to the limited dynamic range of CCD cameras the measured OD saturates, resulting for example in imaging ‘flat-top’ BECs rather than the usual Thomas-Fermi distribution as shown in Figure 10. To get around this issue we typically image with using intensities $I > I_{\text{sat}}$. In order to correctly compute the column density including saturation effects we need a conversion of I_{sat} from mW/cm² to counts per pixel on the CCD camera. We follow the procedure described in [26] find the values of α^* and I_{sat} in counts per pixel. To learn about other effects

such as the recoil momentum from the imaging light that could affect absorption images see [27].

Chapter 4: Making BECs in the Rubidium Lithium apparatus

All the experiments presented in this thesis were performed at the Rubidium-Lithium (RbLi) apparatus at the University of Maryland. The apparatus was designed to produce mixtures of quantum degenerate gases of bosons and fermions. The original plan was abandoned because the cross-species scattering length was found to be repulsive and small ($a_s \approx 20 a_B$) [28] and the nearest Feshbach resonance was measured to occur at the unexpectedly large magnetic field of 1066 G [29]. All our experiments were performed using only ^{87}Rb instead.

The RbLi apparatus is scheduled to be shut down and the construction of a new dual-species apparatus for ^{87}Rb and K^{39} is underway. The RbLi apparatus has been thoroughly described in [7, 8]. Here I only give a brief overview of the apparatus. Additionally I discuss in detail new elements that have been added to the setup and changes that have been implemented and were not previously reported. In Appendix B I discuss the best and the worst aspects of the apparatus.

This Chapter is divided into three sections. In Section 4.1 I give a brief overview of the RbLi apparatus and describe its basic capabilities. In Section 4.2 I describe the experimental sequence used to produce BECs. Finally in Section 4.3 I describe changes and to the RbLi apparatus that have not been reported on previous theses.

4.1 Overview of the RbLi apparatus

The RbLi apparatus is divided into two optical tables. One table contains laser systems that fiber coupled into the main optical table, shown in Figure 1, containing a vacuum system where atoms are cooled to degeneracy. The vacuum system can be divided into three regions: an oven Region where Rb and Li atoms are heated up, a Zeeman slower that acts as a differential pumping stage and an ultra-high vacuum (UHV) region with a glass cell where all the experiments are performed.

4.1.1 Laser systems

We use a total of three lasers to perform laser cooling and imaging of atoms: a cooling laser that addresses the $F = 2 \rightarrow F' = 3$ transition, a repump laser that takes atoms that have decayed into the $F = 1$ state back to $F = 2$ via the $F' = 1$ state and a master laser that provides a frequency reference for both lasers. The frequency of master laser is locked using saturation absorption spectroscopy to the $F = 3 \rightarrow F' = 3$ and $F = 3 \rightarrow F' = 4$ crossover of the D2 line of ^{85}Rb . The repump

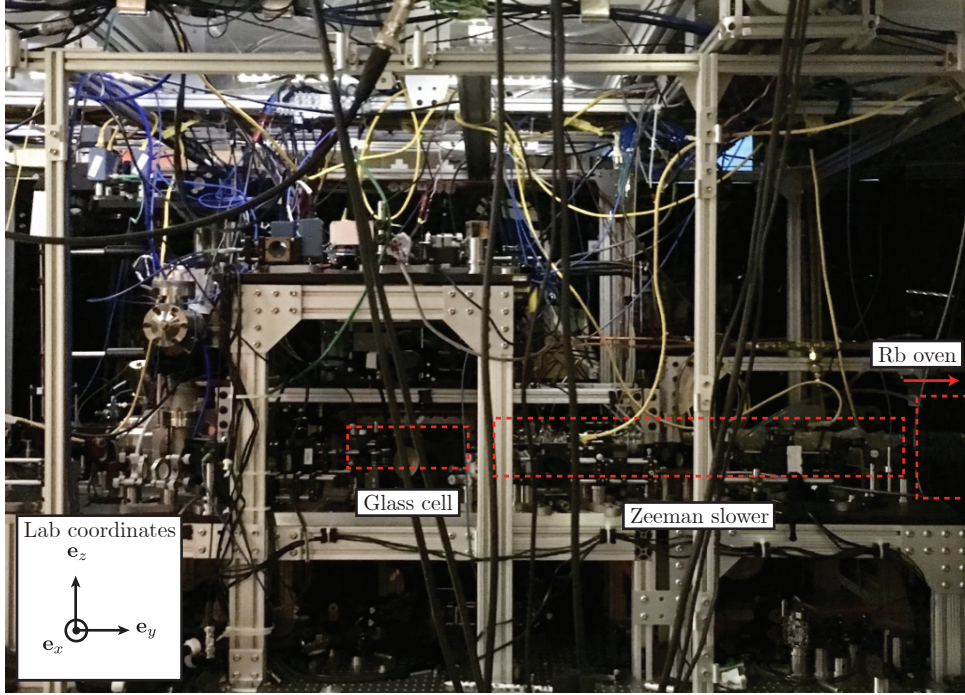


Figure 1: The vacuum system of the RbLi apparatus is divided into an oven, a Zeeman slower and an UHV region containing a glass-cell where all experiments are performed.

and cooling light is split into a beam used for laser cooling in the Zeeman slower and six beams used to create a magneto-optical trap (MOT). The frequencies of each laser with respect to the master laser frequency as well as the frequencies with respect to the transitions in ^{87}Rb can be visualized in Figure 2.

We have two additional lasers that are used to generate potentials for the atoms. The first one is a 30 W 1064 nm IPG Photonics laser located at the main experiment table and that we use to make a cross dipole trap for the atoms. The two dipole beams come from the zeroth and first order of an acusto optic modulator (AOM) and the beams propagate along the $\mathbf{e}_x + \mathbf{e}_y$ and $\mathbf{e}_x - \mathbf{e}_y$ direction (thee lab coordinate system is shown in Figure 1. The other laser system is a Ti:Sapphire laser used to generate Raman transitions and will be described in more detail in Section 4.3.2. Figure 3 shows a simplified diagram with a bird's-eye view and a side view of the apparatus that show all the lasers that are used for cooling, trapping, Raman coupling and imaging.

We can detect atoms using two different imaging systems. The first one is used primarily for diagnostics and it images the yz plane of the atoms from the $+\mathbf{e}_x$ side of the glass cell. The second system looks at the xy plane from bellow the glass cell and is the main system used for data acquisition.

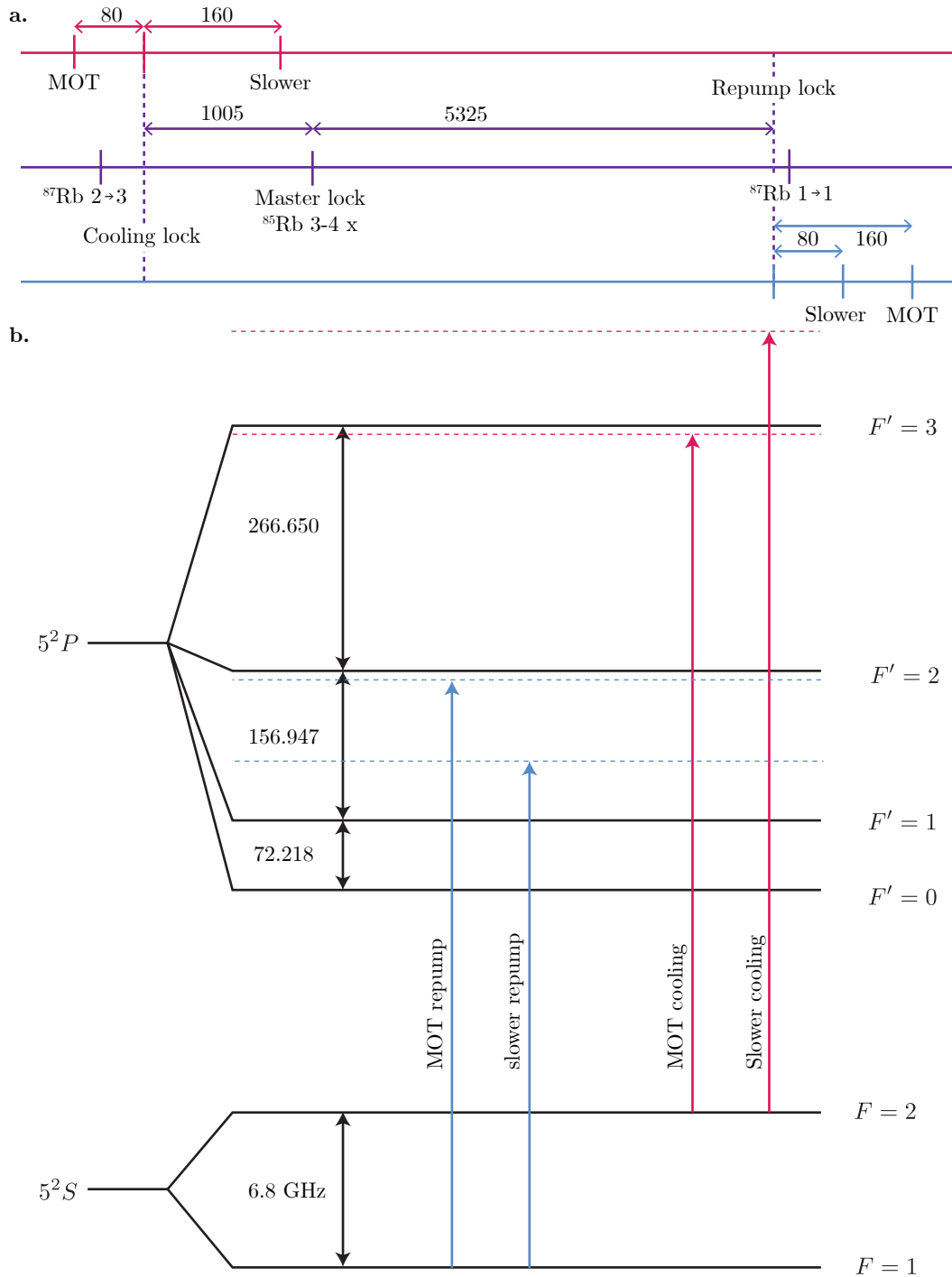


Figure 2: **a.** Cooling and repump frequencies relative to the master laser lock. **b.** Cooling and repump frequencies relative to the ^{87}Rb D2 line transitions.

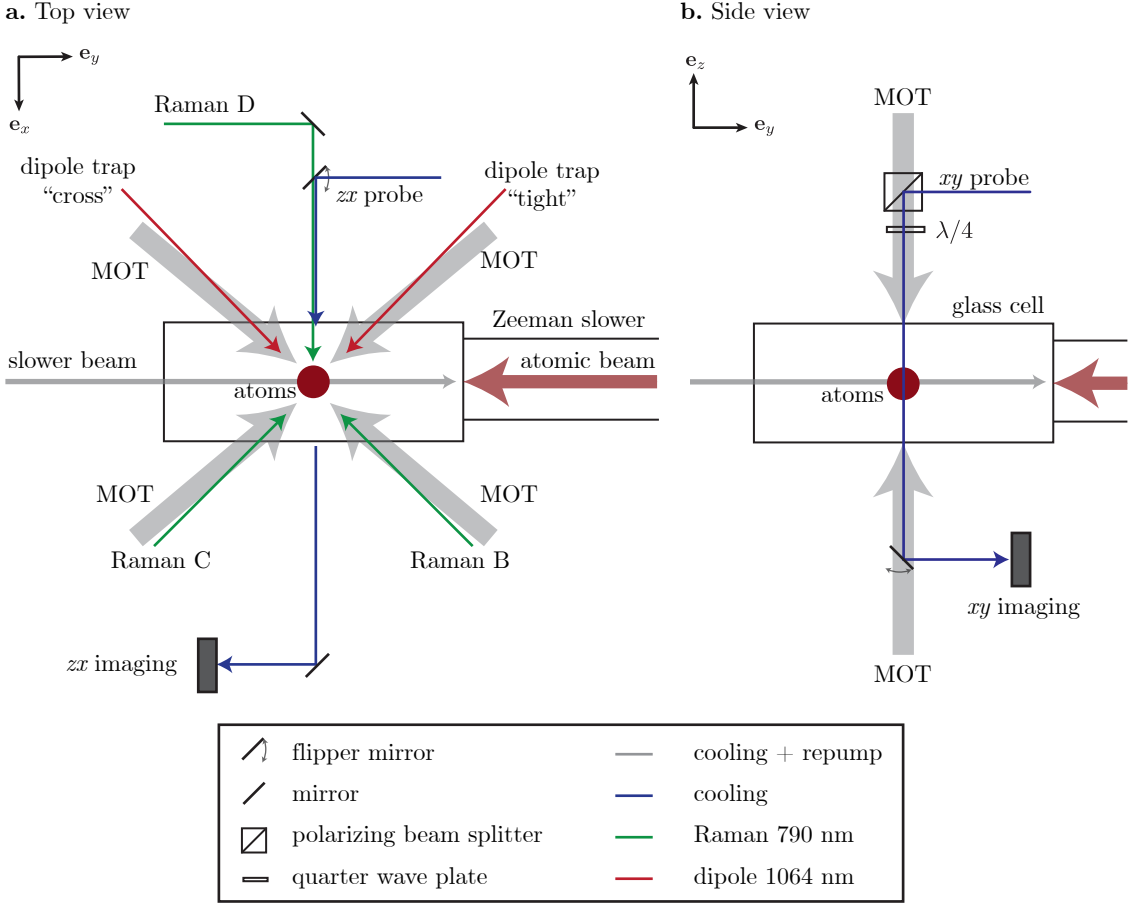


Figure 3: Diagram of the RbLi apparatus as seen from **a.** the top and **b.** the side.

4.1.2 Magnetic field control

The precise control of magnetic fields is essential during the multiple stages in our experimental sequence. We use multiple coils in our experiment as is illustrated in Figure 4. Three pairs of Helmholtz coils in the vicinity of the glass cell generate bias magnetic fields $\mathbf{B} = (B_x, B_y, B_z)$ along \mathbf{e}_x , \mathbf{e}_y and \mathbf{e}_z . Once BECs are produced we typically use bias fields along \mathbf{e}_z to change the Zeeman energy of the different m_F states. One pair of anti-Helmholtz coils generates a strong quadrupole magnetic field along \mathbf{e}_z that is used in the MOT, for magnetic trapping and to separate the different m_F states in time of flight (Stern-Gerlach). An additional set of coils arranged in a ‘clover leaf’ pattern generates small gradients along \mathbf{e}_z , $\mathbf{e}_x + \mathbf{e}_y$ and $\mathbf{e}_z - \mathbf{e}_y$ which allow us to cancel stray magnetic gradients in B_z near the atoms.

The experiment also has the capability of producing oscillatory magnetic fields. A set of coils on a printed circuit board (PCB) produce linearly polarized radio-frequency (RF) magnetic fields either in the \mathbf{e}_y or \mathbf{e}_z direction that are used for RF induced evaporation and to drive transitions between m_F states. There is an

additional setup for producing high-power RF fields with will be described in more detail in Section 4.3.3.

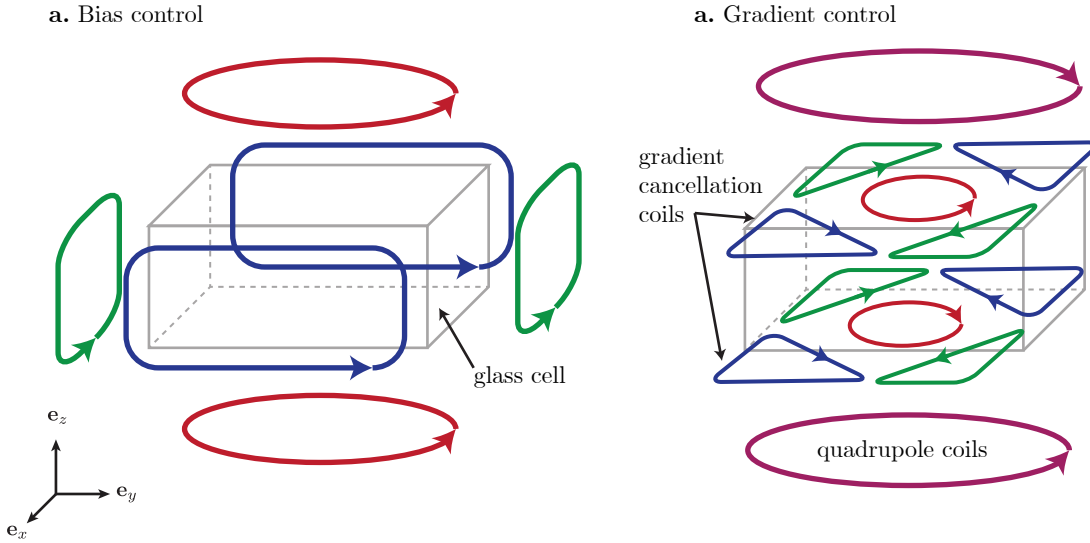


Figure 4: Magnetic coil geometry in the RbLi apparatus. **a.** We use three pairs of Helmholtz coils to produce bias fields along e_x , e_y and e_z . **b.** We have a pair of coils that produce strong quadrupole magnetic fields for the MOT and magnetic trapping. Additionally we have a pair of ‘clover-leaf’ coils to control the gradients in B_z .

4.2 Experimental sequence to make BECs

The production of BECs starts in an oven where Rb atoms are heated to 120°C to produce an atomic beam. The atoms then travel down a Zeeman slower [30] where they are laser cooled and then captured in a MOT. For the MOT we apply a 5.5 A current to the quadrupole coils corresponding to a 15.62 G/cm gradient. The cooling light is blue detuned by $18 \text{ MHz} \sim -3\Gamma$ from the $F = 2 \rightarrow F' = 3$ cycling transition and the repump light is 16 MHz below the $F = 1 \rightarrow F' = 2$ transition. We typically load the MOT for times between 1–5 s before we turn off the Zeeman slower currents and laser beams. In preparation for the molasses stage we do a 30 ms decompression stage where we ramp down the gradient to 10 G/cm and reduce the repump power.

The next step is to perform polarization gradient cooling in optical molasses where the polarization gradient from interfering counter propagating lasers further cools the atoms [31]. For this we completely switch off the quadrupole coils and adjust the bias fields in all three directions so that they are zero at the atoms. During this stage the repump power is kept low and the frequency of the cooling light is decreased to 140 MHz below the MOT frequency for 10 ms. We then completely

turn off the MOT repump light to allow atoms to decay into the $F = 1$ manifold and use a small amount of slower repump light to optically pump atoms into the $|F = 1, m_F = -1\rangle$ magnetically trappable state for a total of 1.5 ms.

Once the atoms are successfully pumped into $|F = 1, m_F = -1\rangle$ we capture them in a magnetic trap with a gradient of 62 G/cm and compress them by increasing the current in the coils until we reach a gradient of 160 G/cm in 300 ms. In the magnetic trap we perform RF induced evaporation by turning on an RF field polarized along \mathbf{e}_y with frequency of 24 MHz, which transfers the hotter atoms at the edges of the trap into the $m_F = 0$ state which is not magnetically trappable. We then perform an exponential ramp from the initial frequency to a final frequency of 4.5 MHz in 1 s.

For the final stage of evaporative cooling we transfer the atoms from the magnetic trap into an optical dipole trap. We start by turning on only the ‘tight’ arm of the trap at full power (about 11 W) and slowly decompressing the quadrupole trap to 45 G/cm in 1.5 s. We then turn on the second ‘cross’ beam in 1 s; splitting the power so that there the power split between the tight and cross beams is about 70 – 30%. As the cross dipole beam is being turned on we ramp the quadrupole field further down to 14 G/cm, slightly above the value necessary for the trap to suspend atoms against gravity. We simultaneously shift the bias field along \mathbf{e}_z to align the center of the quadrupole trap to the dipole trap.

We evaporate the atoms in the dipole trap in two stages. First we exponentially ramp down the power to about 20% of its initial power in 1.5 s (time constant = 0.5 s). Before the final evaporation stage we completely turn off the quadrupole trap in 1 s. Finally, we perform a second exponential ramp where the power is dropped to about 30% of the intermediate power in 2 s (time constant = 1 s). The slow ramps ensure that there is enough time for the atoms to thermalize as they evaporate. During the second evaporation stage the atoms reach the critical temperature for Bose-Einstein condensation and we are able to produce BECs with about 4×10^4 atoms in the $|F = 1, m_F = -1\rangle$ state. At this point we can prepare different m_F states and set the Zeeman splitting between levels using the techniques described in the following sections.

4.2.1 Adiabatic rapid passage

[Consider moving these two subsections to the previous Chapter...]

We prepare different m_F states within the $F = 1$ manifold using an adiabatic rapid¹ passage protocol (ARP) which is based on the Landau-Zener model [32]. The technique relies on preparing dressed states; eigenstates of the atomic Hamiltonian with an oscillatory field magnetic field (RF or microwaves for our experiments). To perform ARP with RF we set the frequency of the field ω_{RF} so that it matches the Zeeman splitting between the $m_F = -1$ and $m_F = 0$ states for a target bias field $B_0 \mathbf{e}_z$.

We start with atoms in $m_F = -1$ and at a bias field $B_i \approx B_0 - 380 \text{ mG}$

¹Rapid with respect to the spontaneous emission rate of the excited state being coupled.

$(\delta \approx 30 \text{ kHz})$. We ramp an $\Omega = 20 \text{ kHz}$ RF field and angular frequency ω_{RF} in 50 ms, effectively mapping atoms in the $m_F = -1$ state into the ground state of the RF Hamiltonian as shown in Figure 4.2.1a. We then sweep the detuning by linearly changing the bias field. As the detuning is changed, the state decomposition of the ground state is modified and as long as the rate of change in detuning is small compared to Ω_{RF}^2 (or small compared to the gap in Figure 4.2.1a) the system will adiabatically follow the ground state. After the detuning sweep the RF field is abruptly turned off, projecting the RF eigenstates into the m_F states. In Figure 4.2.1 we set $\omega_{\text{RF}} = 23 \text{ MHz}$ and when the Zeeman splitting between $m_F = -1$ and $m_F = 0$ is equal to ω_{RF} we observe an equal superposition of both states and if the detuning is swept beyond resonance we can reliably prepare the $m_F = 0$ state. In general it is necessary to look at the eigenstates of the three-level RF Hamiltonian

$$\hat{H}_{\text{RF}} = \begin{pmatrix} -\delta & \Omega_{\text{RF}}/2 & 0 \\ \Omega_{\text{RF}}/2 & -\epsilon & \Omega_{\text{RF}}/2 \\ 0 & \Omega_{\text{RF}}/2 & \delta \end{pmatrix}, \quad (4.1)$$

but for large quadratic Zeeman shifts as is usually the case in our experiments we can only look at an effective two-level system.

In order to keep the bias fields as stable as possible we also synchronize the timing of our experiments to the 60 Hz line; this step is performed in different stages of the experiment but perhaps were we have noted it has the biggest impact is right before ARP. For additional magnetic field control and stabilization we use a technique using microwave assisted partial transfer absorption imaging described in the following section.

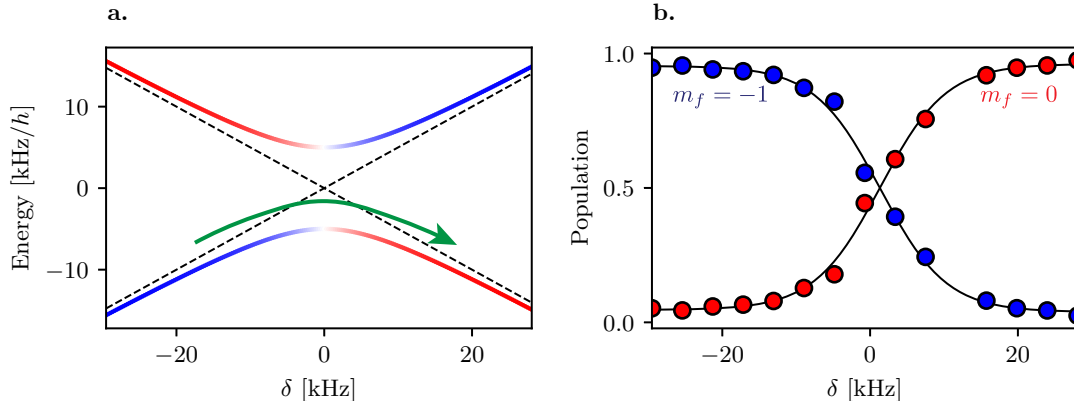


Figure 5: **a.** Eigenenergies and eigenstate decomposition of an RF dressed Hamiltonian for a two-level system (Equation 3.35) with $\Omega = 10 \text{ as}$ a function of detuning. The eigenstates are linear combinations of $m_F = -1$ and $m_F = 0$ (red and blue respectively). **b.** Population in the m_F states for different values of detuning

4.2.2 Magnetic field stabilization with microwave assisted partial transfer absorption imaging

Our experiments are very sensitive to changes in the environmental magnetic field. In the past we used flux gate sensors (**Stefan-Mayer** model FL1-100 f) in the apparatus to feedback and stabilize the magnetic field (see [8]). These sensors are a useful tool, however due to space constraints we were not able to measure the fields close to the atoms and additionally the range of magnetic fields that they operate at is small (only 1 G, we typically operate at $B > 10$ G). We built a 6.8 GHz microwave system (see Section 4.3.4) so that we could use the atoms themselves as sensors of magnetic field.

The method relies in transferring a small fraction of atoms into the $F = 2$ manifold where they can be imaged without the use of repump light and therefore minimally disturbing the remaining atoms in $F = 1$. We apply two microwave pulses for a total time τ with frequency $\omega_0 - \delta_{\pm}$ where $\delta_{\pm} = \pm 1/(2\tau)$. We typically set ω_0 equal to the Zeeman splitting between the $|F = 1, m_f = -1\rangle$ and $|F = 2, m_f = -2\rangle$ states and we set the coupling strength $\Omega_0 \ll 1/\tau$ such that only about 5% of the atoms are transferred by each pulse. We image the transferred atoms following each pulse using absorption imaging and from the measured densities we calculate the imbalance

$$n_{\text{imb}} = \frac{n(\delta_+) - n(\delta_-)}{n(\delta_+) + n(\delta_-)} \quad (4.2)$$

which gives us a signal that is both insensitive to fluctuations in the number of

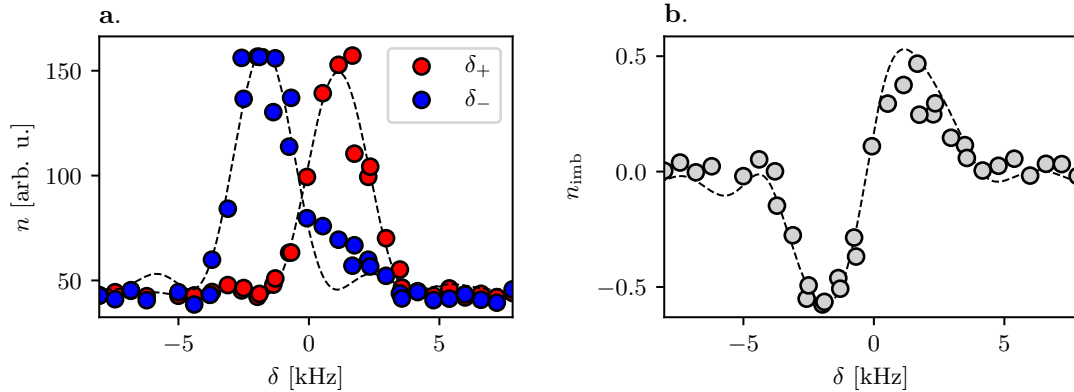


Figure 6: Magnetic field stabilization using microwave assisted PTAI. **a.** Population transferred into $|F = 2, m_F = -1\rangle$ from $|F = 1, m_F = -1\rangle$ as a function of bias magnetic field (global detuning δ). Each microwave pulse was $\tau = 250 \mu\text{s}$ and detuned by $\delta_{\pm} = \pm 1/(2\tau)$ to transfer a small fraction of atoms from $|F = 1, m_F = -1\rangle$ into $|F = 2, m_F = -1\rangle$. **b.** Error signal calculated using the transferred atoms by each pulse. We lock the magnetic field to the ~ 5 kHz (~ 7 mG) wide linear portion of the signal.

atoms and linearly sensitive to changes in magnetic field². We use this error signal both to monitor the magnetic field before performing experiments and cancel long term drifts in the field. In most cases, we chose the states $|F = 1, m_F = -1\rangle$ and $|F = 2, m_F = -2\rangle$ as their relative energies are the most sensitive to changes in magnetic field. Figure 6a shows the transferred atoms by each microwave pulse for different values of bias magnetic field and Figure 6b shows the imbalance. The microwave frequency ω_0 is on resonance with the $|F = 1, m_F = -1\rangle \rightarrow |F = 2, m_F = -2\rangle$ transition when both pulses transfer the same number of atoms.

In [33] we studied partial transfer absorption imaging as minimally destructive technique for imaging ultracold atoms. See Chapter 6 for an alternative solution for dealing with magnetic field noise.

4.3 Upgrades to the RbLi Machine

4.3.1 Master laser system

Previously we used a **New Focus Vortex II** TLB-6900 extended cavity diode laser as our master laser and a home made saturation spectroscopy setup using a Rb glass cell (see [7, 8]). The frequency of this laser was not very stable and the laser would constantly get out of lock. We replaced the old master laser with a **Vescent photonics DBR Laser Module System** which uses a distributed Bragg reflector laser diode with no external cavity and is therefore very mechanically stable. The frequency of the laser is stabilized and controlled using the D2-210 spectroscopy module and D2-125 laser servo. The master laser system is considerably simplified as can be seen in Figure 7.

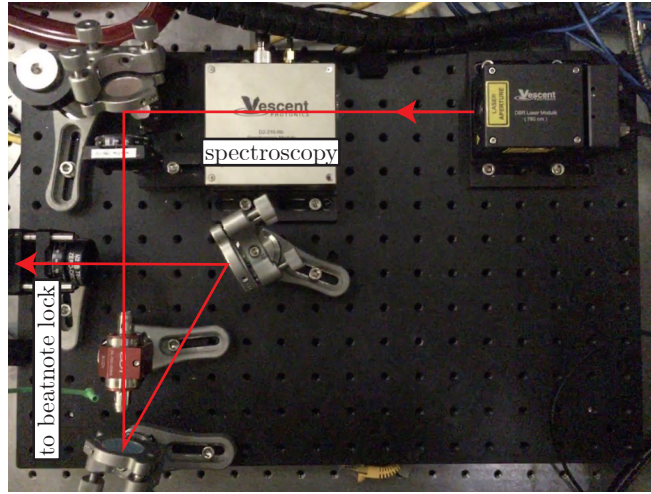


Figure 7: Master laser system. We replaced the old Vortex II laser with a Vescent photonics DBR Laser Module System that is considerably more stable.

²A single pulse on resonance is quadratically sensitive to detuning (see Equation 3.34)

4.3.2 Raman laser system

The RbLi apparatus has a laser system with wavelength close to 790 nm that is used to generate Raman induced transitions and spin-dependent potentials (see Section 3.3.2). The original Raman laser system consisted of a Toptica DL Pro laser seeding a tapered amplifier mounted on a homemade copper holder. This laser system was replaced by an M squared Ti:Sapphire laser (SolsTiS-400-SRX-F) that is pumped by a 532 nm IPG GLR30 laser. We typically operate the pump laser at 14.5 W, a fraction of this light is redirected into the path of a 1D optical lattice and the remaining power is used to pump the Ti:Sahprie laser. We switched to using a Ti:Sapph laser because of its wide range of tunable wavelengths in the near infrared (725 – 875 nm) and its high power output. Figure 8 shows the typical dependence of the Ti:Sapph output power as a function of pump power.

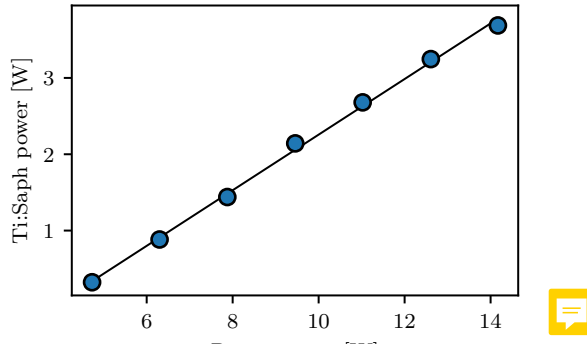


Figure 8: Ti:Sapphire laser output as a function of pump power. This data was taken when the laser was being setup for the first time. The alignment of the laser cavity was optimized to produce maximum power at 15 W pump power. The output power is proportional to the pump power $P_{\text{out}} \approx 0.364P_{\text{pump}}$.

The output of the laser is split into 3 different Raman beams. The frequency and power of each beam is independently controlled using IntraAction ATM-801A2 AOMs centered at 80 MHz. We drive the AOMs using homemade drivers made from the Minicircuits components listed in Table 4.1 and Novatech Model 409B direct digital synthesizer (DDS) to generate an RF signal at the desired frequency. The components are arranged as is shown in Figure 10: we control the amplitude of the RF signal using a mixer connected to a DC signal and the switch can turn off the signal in less than 1 μ s using a TTL signal. We fiber couple the light using single mode optical fibers (non-polarization maintaining) with FC/APC type connectors at the input (laser side) and FC/PC at the output (experiment side). We made this choice so to implement a phase lock that would cancel phase noise added by the fibers. The idea behind this method is that a small fraction of the fiber coupled light is reflected at the flat cut edge of the optical fiber and coupled back where it can be heterodyne probed with the input light (see Figure 9), our implementation described in Section 3.6.3 of [34]. We control the polarization of the light using

polarization controlling paddles (Thorlabs FPC030 and Thorlabs FPC560) which produce a controllable amount of stress in the fibers that changes their birefringence, a method that we have found to be much more stable than using polarization-maintaining fibers even when the polarization of the light is properly aligned to the fiber slow/fast axis. None of the experiments presented in this thesis used the phase lock but the experiments described in Chapter 8 were performed using the new Raman laser system. Figure 9 shows a diagram of the Raman optics as well as the 532 nm optical lattice optics which are shared on the same breadboard.

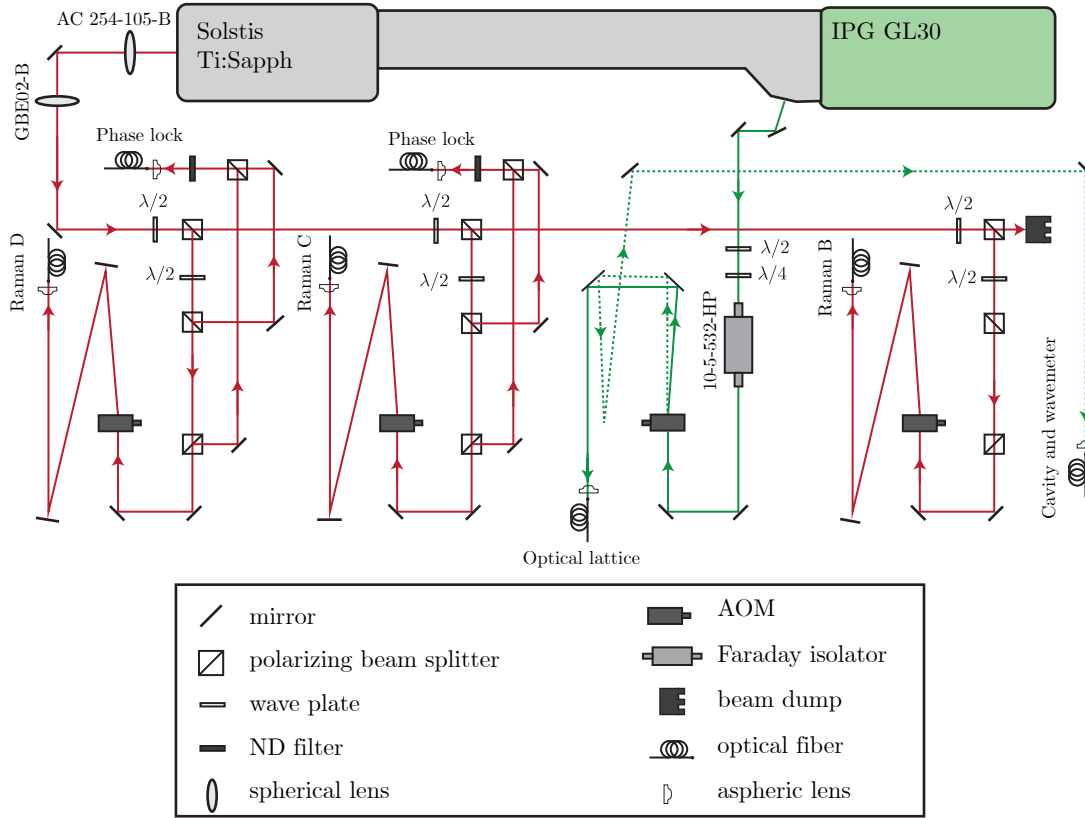


Figure 9: Optical layout of Raman and optical lattice lasers. The Ti:Sapphire laser provides tunable infrared light that we use for three different Raman beams. The beams labeled as ‘Raman C’ and ‘Raman D’ can be phase stabilized. A small fraction of the green pump laser is used to produce a blue-detuned 1D optical lattice.

4.3.3 High power RF system

The experiments described in Chapters 6 and 8 required the use of high power RF magnetic fields to achieve coupling strengths at the atoms $\Omega \sim 100 - 200$ kHz. To do so we built a resonant circuit with a coil close to the atoms. After multiple attempts to build a resonant coil either on a PCB (similar to the coil used for RF

Table 4.1: List of AOM driver components

Part number	Description
ZHL-1-2W	2 W amplifier
ZAD-3+	Mixer
ZYSWA-2-50DR	Digital switch

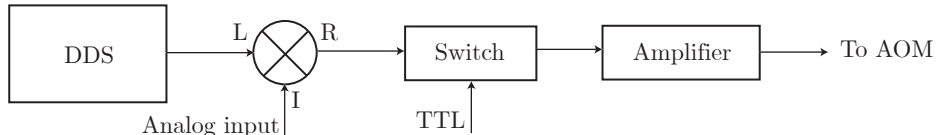


Figure 10: Setup used to drive the AOMs controlling the power and frequency of Raman beams. A similar setup is used to drive a coil used to generate high-power RF fields at the atoms.

induced evaporation, see [7, 8]) or winding some wires with the right dimensions we found that the product that worked best for our needs was a wireless power charging receiver coil (**Würth Elektronik Digikey part number 732-5646-ND**) shown in the bottom panel of Figure 4.3.3a. The coil has a self resonant frequency at 22 MHz and a Q-Factor of 45. It has an inner diameter of 1.62 cm and an outer diameter of 2.8 cm, just the right size for us to place it snugly next to the glass cell (on the $-e_x$ side) with minimal perturbations to the laser beams in its vicinity (it only slightly clips one MOT beam).

The loop is mounted on the PCB shown in Figure 11. The board has two connections: the top one in Figure 11 has a small loop used as a pickup antenna that we attach to a power detector **Minicircuits ZX47-40-S+** to monitor the the antenna and the bottom lines have pads that can be used to make an impedance matching network.

We used a vector network analyzer (VNA) to help us perform the impedance matching. The VNA sends a small amplitude frequency into the circuit and measures the amplitude and phase of the reflected power from which the impedance can be inferred. Figure 12a shows the reflected power as a function of frequency for a test circuit and Figure 12b shows the complex valued impedance as a function of frequency displayed on a Smith chart. The Smith chart is a helpful way to visualize the impedance of a circuit: the black circles correspond to constant resistance, with the right most point corresponding to an open circuit (infinite resistance) and the largest circle corresponding to a short circuit (zero resistance). The arcs correspond to constant reactance; the horizontal axis corresponds to zero reactance ($\text{Im}(Z) = 0$), the top arcs correspond to $\text{Im}(Z) > 0$ and the lower arcs to $\text{Im}(Z) < 0$. The circuit is impedance matched when $Z = 50 \text{ Ohm}$ (the center of the Smith chart), the standard

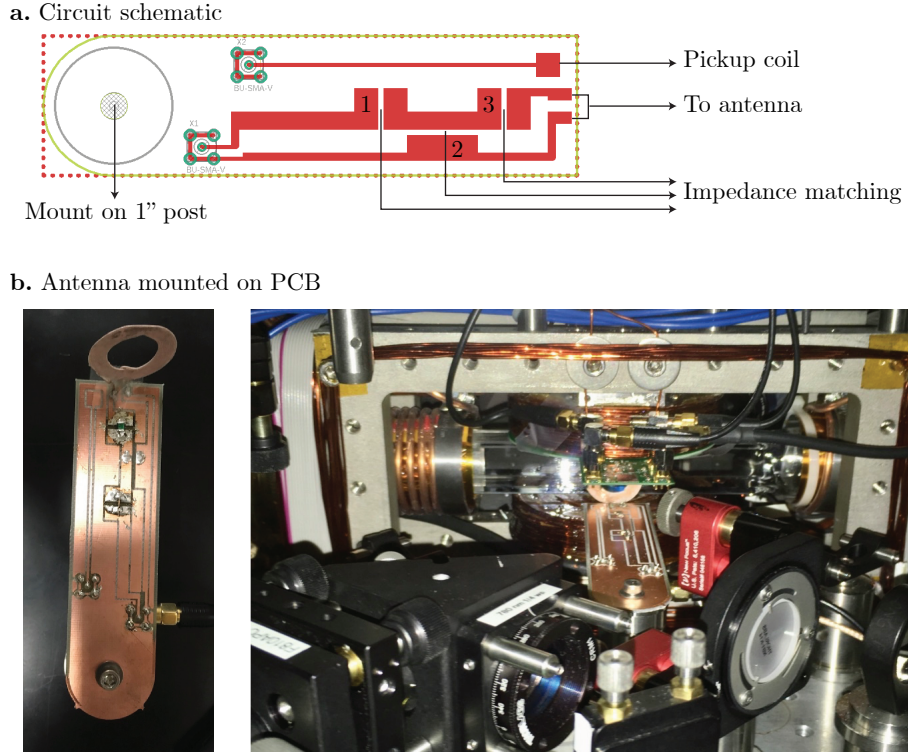


Figure 11: We use a commercial resonator with an impedance matching network to produce high power RF fields. **a.** Diagram of the impedance matching network. **b.** A picture of the resonator mounted on a PCB. We place this device as close to the atoms as possible next to the glass cell.

value of RF transmission lines. We tested different components on the pads until we found a peak in reduced transmission at the desired frequency. It is also important to note that it was important that the circuit was installed in its final location in the experiment when measuring the impedance as the other parts in the vicinity of the antenna can shift the resonant frequency.

The driving electronics are very similar to the AOM drivers described in Section 4.3.2. The only difference is we use a 30 W amplifier ([Minicircuits LZY-22+](#)) instead of the smaller amplifiers needed to drive the AOMs.

4.3.4 6.8 GHz microwave system

Our apparatus now has a 6.8 GHz microwave system that allows us to transfer atoms between the $F = 1$ and $F = 2$ ground hyperfine manifolds of ^{87}Rb . We mostly use this system to stabilize the bias magnetic field along \mathbf{e}_z at the atoms using microwave assisted partial transfer absorption imaging (PTAI) (Section 4.2.2). A list of components used to in the setup is presented in Table 4.2 and a diagram of the connections is displayed in Figure 13.

The SRS generator serves as a source of a fixed frequency and amplitude

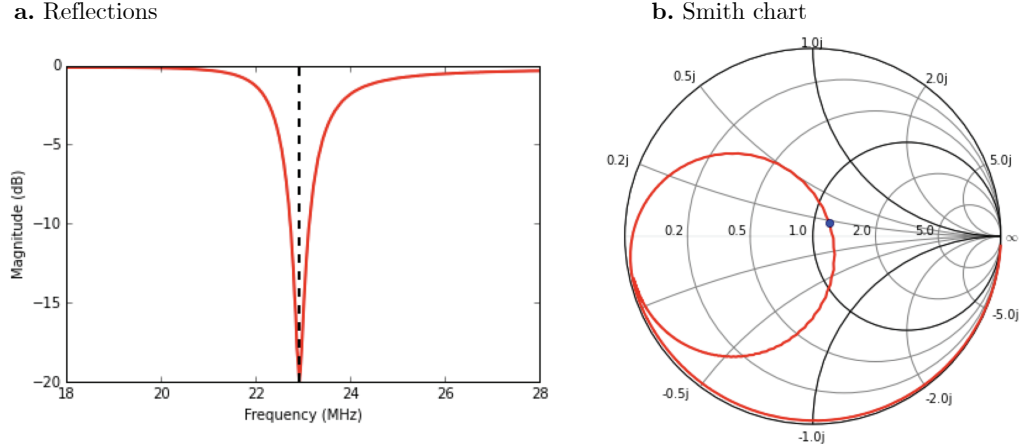


Figure 12: Impedance matching of high power RF antenna. **a.** Reflected power as a function of frequency. **b.** Impedance as a function of frequency, visualized on a Smith chart.

signal. We control the frequency by mixing a programmable ~ 100 MHz signal from a Novatech into a double balanced mixer; the RF signal can be turned on or off using a TTL switch. The amplitude is controlled by commanding 0–6 V signal from the control computer into an attenuator. The signal is amplified by +43 dB using an amplifier mounted on a water cooled plate. The microwave signal is broadcast to the atoms using a horn antenna. In order to get a coupling microwave coupling strength of the order of 10 kHz or larger it was important to place the horn as close to the atoms as possible and to impedance match the transmission line to maximize the radiated power. We additionally use a circulator that prevents any reflected power to go back into the amplifier. We use couplers at different locations to monitor the performance of the system. The last coupler and the circulator of the system are connected to a power detector that outputs a DC signal proportional to the microwave power. The impedance is tuned with a stub tuner by changing the length of the stubs so that the reflected power measured at the exit port of the circulator is minimized at the desired frequency of operation.

4.4 Computer control and data acquisition

There have been two main changes in our computer control and data acquisition system. We have transitioned from using a LabVIEW based control system to a Python based control system, The `labscrip` suite [35]. With the previous control software the lab devices were programmed using a graphic interface. `Labscrip` instead uses a hybrid approach in which the experimental sequences are text based scripts. The use of scripted programming has given us more flexibility and modularity for programming experiments and additionally it is now very easy

Table 4.2: 6.8 GHz microwave system components

Part number	Description
SRS SG384	Signal generator
Narda 4014C-30	Directional coupler
Marki IRW0618	Mixer
Minicircuits VBFZ-6260-S+	Bandpass filter 6 – 8 GHz
Herley D1956	Voltage controlled attenuator
MSI MSH-5727901	46 dB gain amplifier
Narda 4014C-30	Circulator
Minicircuits ZX47-40-S+	Power detector
Maury microwave 1819C	Stub tuner
ZYSWA-2-50DR	Digital switch

to do multi-dimensional parameter scans. Each experimental shot is saved in a Hierarchical Data Format version 5 file (HDF5). The file includes images from cameras, oscilloscope traces and analog inputs as well as copy of the script used in the experiment and the values of all of the parameters used. This has been a great upgrade as we no longer rely on the person running an experimental sequence pushing the ‘save’ button and thoroughly documenting the experiment in question³.

The other upgrade worth mentioning is replacing our old Flea3 CCD camera with a Mako G-030 camera from Allied Vision. With this new camera the time between two consecutive shots can be as short as $96\ \mu\text{s}$ (we used to wait $\sim 30\ \text{ms}$ with the Flea3 camera), greatly reducing the effect of mechanical vibrations in the experiment that produce fringes in the absorption images. In our experimental sequence the probe and atoms images are separated by $150\ \mu\text{s}$, which is not enough time for the atoms in the first absorption image to be cleared out. We therefore had to change the order in the absorption imaging protocol: first we take a picture of the probe which is 6.8 GHz detuned and minimally disturbs the atoms, we then apply repump light during the $150\ \mu\text{s}$ interval in between the images to transfer atoms into $F = 2$ and then take the absorption image of the atoms. Figure 14 shows the OD computed using both cameras with no atoms present. When there is a long interval in between the two images the probe captured on the camera changes, leading to the fringes shown in Figure 14a. In contrast for probe images captured within short interval the main noise contribution is shot noise as can be seen in Figure 14b. The addition of this camera was essential to get a better signal to noise ratio in the experiments reported in Chapter 8.

³As I have been digging into old data, I greatly wish we had this feature sooner.

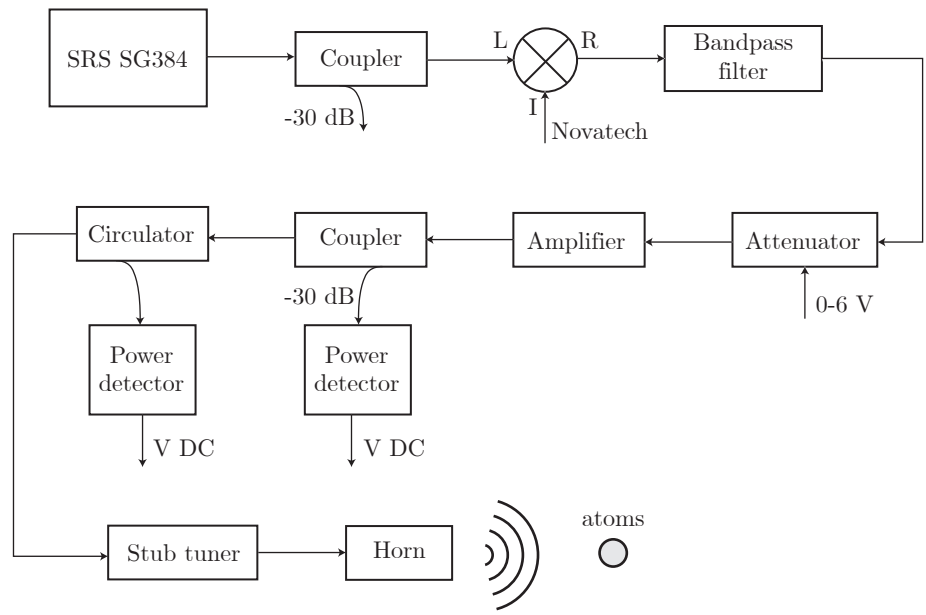


Figure 13: Schematic of 6.8 GHz microwave system.

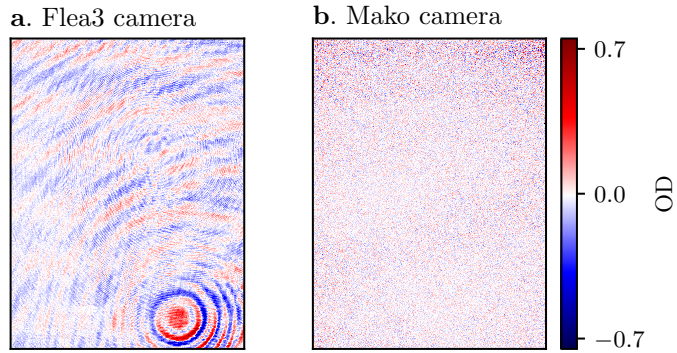


Figure 14: OD computed using two consecutive probe images without atoms. **a.** With the Flea3 camera images are spaced by ~ 30 ms. Changes in the probe result in fringes in the OD. **b.** With the Mako camera images are spaced by $\sim 150 \mu\text{s}$. The main source of noise in the OD is shot noise.

Chapter 8: Unconventional topology with a Rashba SOC quantum gas

As I mentioned in the previous Chapter topological order is present in a wide range of physical systems and is quantified by integer valued topological invariants such as the Chern number. In this Chapter I describe a system with Rashba-type spin-orbit coupling whose topological invariants can take half-integer values. If the concept of half-integer invariants does not sound odd, think of a donut with half a hole.

Ultracold atomic systems are an emerging platform for engineering topological lattices, from the Harper-Hofstadter model [96, 97], the Haldane model [98], to the Rice-Mele model [99, 100] as well as assembling spin-orbit coupled lattices without analogues in existing materials [101, 102]. However, experimental realizations of topological materials have mostly focused on engineering different topological bands (with different Berry curvatures) in lattice systems, where the BZ is always a torus. Here I show that by eliminating the lattice potential and thereby changing the BZ from \mathbb{T}^2 to \mathbb{R}^2 , i.e. from a torus to a Cartesian plane, it is possible to create topological branches of the dispersion relation with half-integer Chern number.

The experiments presented here combine the experimental techniques that were presented in Chapters 5 and 6, additionally I use the key concepts of topology described in Chapter 7. This Chapter is organized in the following way: First I give a general overview of Rashba SOC and describe theoretical proposals for engineering this type of coupling in ultracold atom systems. Then I describe our experimental implementation of Rashba SOC in the lab using a trio of Raman coupled CDD states and validate our quantum engineering using Fourier transform spectroscopy. Finally I describe a quantum state tomography procedure to measure the eigenstates of our system, from which we can directly obtain the Chern number.

To avoid confusion between dressed state xyz labels and Cartesian coordinates, in this Chapter I will use the numbers 1, 2, 3 to label the coordinates $\mathbf{e}_x, \mathbf{e}_y, \mathbf{e}_z$ and the letters x, y, z to label clock state parameters.

8.1 Rashba spin-orbit coupling

Rashba SOC [18] appears in condensed matter systems where electrons are confined in a 2D plane and experience an intrinsic out-of-plane electric field. If the electron's momentum is given by $\hbar\mathbf{k} = \hbar(k_x\mathbf{e}_x + k_y\mathbf{e}_y)$ and the electric field is $\mathbf{E} = E\mathbf{e}_z$, in the electron's moving frame there will be a momentum dependent magnetic field $\mathbf{B}_{\text{SOC}} = -\hbar\mathbf{k}/m \times \mathbf{E}/c^2 = \hbar E/mc^2(-k_y, k_x, 0)$. The interaction

between the electron's spin with this field through the magnetic Zeeman interaction $-\mu \cdot \mathbf{B}_{\text{SOC}}$ gives rise to the SOC Hamiltonian

$$\hat{H}_{\text{SOC}} = \frac{2\alpha}{m}(k_y\hat{\sigma}_x - k_x\hat{\sigma}_y) \quad (8.1)$$

where $\alpha = g\mu_B E/c^2$, g is the electrons gyromagnetic ratio, μ_B is the Bohr magneton and $\hat{\sigma}_i$ are the Pauli matrices.

As can be seen in Figure 1, the Rashba dispersion relation is characterized by having a Dirac point located at $\mathbf{k} = 0$ (see Section 7.5) and a degenerate ground state that is described by the ring $k_x^2 + k_y^2 = \alpha^2$. If we combine Equation 8.1 with the free particle Hamiltonian the Hamiltonian can be written as $\hat{H} = (\hbar\mathbf{k} - \hat{\mathbf{A}})^2/2m$ where $\hat{\mathbf{A}} = \alpha(\hat{\sigma}_y\mathbf{e}_x - \hat{\sigma}_x\mathbf{e}_y)$ can be interpreted as a (matrix valued) non-Abelian gauge potential [103] whose elements do not commute. This term is closely related to the Berry connection discussed in Section 7.3. This non-Abelian gauge potential in combination with the Dirac point hints at us that a system with Rashba SOC has non-trivial topology.

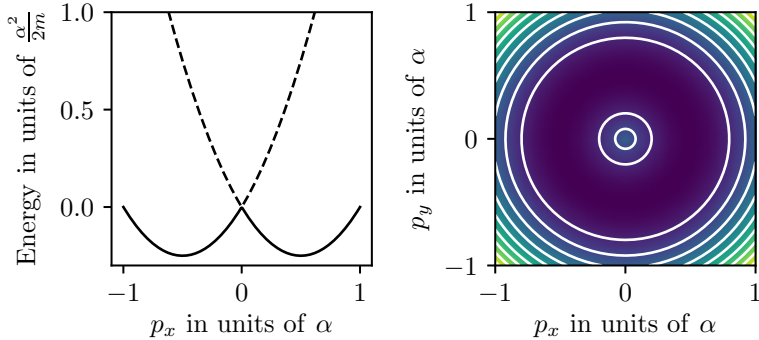


Figure 1: The Rashba dispersion relation has a Dirac point located at $\mathbf{k} = 0$ and a degenerate ground state that is described by the ring $k_x^2 + k_y^2 = \alpha^2$. [TODO: Might be nice to add the 'hedgehog' field as well]

SOC is a necessary ingredient for realizing \mathbb{Z}_2 topological insulators and the quantum spin-Hall effect. Furthermore, the degeneracy of the ground state single particle eigenstates could open the possibility of studying strongly correlated phases in the presence of interactions for systems of both fermions and bosons [104–106]. Using ultracold atomic systems to engineer SOC, and in particular Rashba type SOC, has been a longstanding goal [20].

8.2 Rashba SOC for neutral atoms

Proposals for engineering Rashba type SOC in neutral atoms consist in using lasers to link internal states of an atom with its linear momentum. In order to achieve

non-trivial gauge potentials it is necessary to couple $N \geq 3$ levels (see [107]). I will describe the proposal by [108] which considers a ‘ring coupling’ which is shown in Figure 2 for the case of $N = 3$. The states $|j\rangle$ represent internal atomic states and they are linked to each other with complex valued matrix elements $\frac{\Omega_j}{2} e^{i\mathbf{k}_j \cdot \mathbf{x}}$, where \mathbf{k}_j is a momentum transfer associated with the $|j\rangle \rightarrow |j+1\rangle$ transition and $\Omega_i = e^{i\phi_i} |\Omega|$ represents the coupling strength. We require that $\sum \mathbf{k}_i = 0$ so that no momentum is transferred when a closed loop $|1\rangle \rightarrow |2\rangle \dots \rightarrow |N\rangle \rightarrow |1\rangle$ is completed. For this case the \mathbf{k}_i momenta vectors can be written as $\mathbf{k}_j = \mathbf{K}_{j+1} - \mathbf{K}_j$, and we make $\mathbf{K}_j = k_L \sin(2\pi j/N) \mathbf{e}_x + k_L \cos(2\pi j/N) \mathbf{e}_y$, corresponding to the vertices of an N sided regular polygon. We can further make a gauge transformation such that we can replace the phases ϕ_i associated to each coupling with $\bar{\phi} = \sum_i \phi_i / N$.

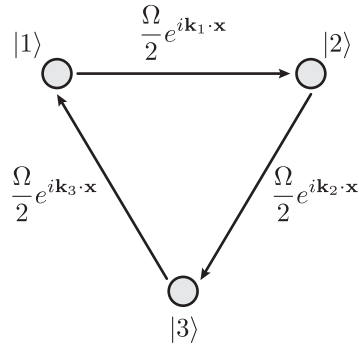


Figure 2: The Rashba ring coupling. To generate Rashba SOC in a system of cold atoms it is necessary to cyclically couple $N \geq 3$ internal states such that the transition $|j\rangle \rightarrow |j+1\rangle$ has a momentum transfer \mathbf{k}_j and $\sum_j \mathbf{k}_j = 0$ such that there is no momentum transfer for a closed loop $|1\rangle \rightarrow |2\rangle \dots |N\rangle \rightarrow |1\rangle$. The ring coupling combined with the free particle Hamiltonian give rise to a 2-level subspace that can be described to first order by the Rashba Hamiltonian

The Hamiltonian describing this coupling along with the kinetic term is

$$H_{j,j'} = \frac{\hbar^2 k^2}{2m} \delta_{j,j'} + \frac{\Omega}{2} (e^{i(\bar{\phi} + \mathbf{k}_j \cdot \mathbf{x})} \delta_{j,j'+1} + \text{h.c.}), \quad (8.2)$$

and after applying the unitary transformation $U_{j,j'} = \exp[i\mathbf{K}_i \cdot \mathbf{x}] \delta_{j,j'}$ ¹ it gets transformed to

$$H_{j,j'} = \frac{\hbar^2}{2m} |\mathbf{q} + \mathbf{K}_j|^2 \delta_{j,j'} + \frac{\Omega}{2} (e^{i\bar{\phi}} \delta_{j,j'+1} + \text{h.c.}), \quad (8.3)$$

where I have replaced the momentum \mathbf{k} by the quasimomentum \mathbf{q} . The off diagonal terms of Equation 8.3 can be related to a 1D periodic tight-binding Hamiltonian with hopping elements $\Omega/2$ where the internal states $|j\rangle$ represent lattice sites and completing one loop corresponds to gaining a ‘flux’ of $N\bar{\phi}$. To visualize how the

¹This transformation is equivalent to applying a state dependent momentum boost $\mathbf{k} \rightarrow \mathbf{k} + \mathbf{K}_j$

Rashba Hamiltonian emerges from this coupling scheme, it is helpful to write the Hamiltonian in a basis that is conjugate to the index j ²

$$|l\rangle = \frac{1}{\sqrt{N}} \sum_{j=1}^N e^{i2\pi jl/N} |j\rangle \quad (8.4)$$

where the index l is analogous to the crystal momentum index for a Bloch Hamiltonian. In this new basis, terms in the diagonals are displaced to the off-diagonal and likewise terms in the off diagonals are displaced to the diagonal. Under this basis the Hamiltonian starts looking very much Rashba-like

$$H_{l,l'} = \left[\frac{\hbar^2}{2m} (q^2 + k_L^2) + E_l \right] \delta_{l,l'} + \frac{\hbar^2 k_L}{m} [(iq_x + q_y)\delta_{l-1,l'} + \text{h.c}], \quad (8.5)$$

where $E_L = 2\hbar\Omega \cos(2\pi l/3 + \bar{\phi})$ correspond to the eigenenergies when $q = 0$. The phase $\bar{\phi}$ can be tuned such that a pair of states with consecutive l index become degenerate, indicating the presence of a Dirac point at $q = 0$. Figure 3 shows the energies E_l for $N = 3$ and $\bar{\phi} = 0$.

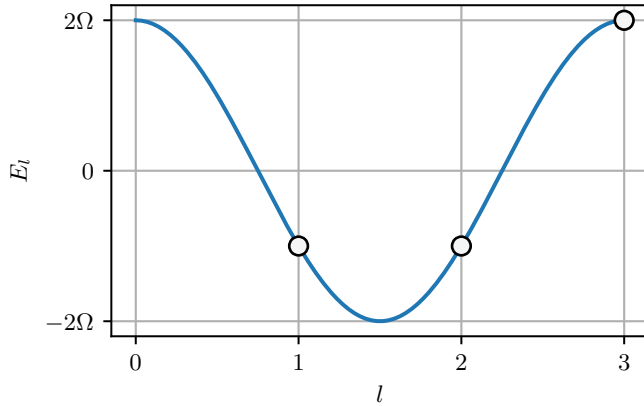


Figure 3: Eigenenergies of Equation 8.5 for $q = 0$ for $N = 3$ and $\bar{\phi} = 0$. For this particular choice of phase, the energies of the $l = 1$ and $l = 2$ states become degenerate

We can consider the degenerate states as pseudospins which are described to zeroth order by the Rashba plus free particle Hamiltonian

$$\hat{H}^{(0)} = \frac{\hbar^2 q^2}{2m} + \frac{\hbar^2 k_L}{m} (\hat{\sigma}_x q_y - \hat{\sigma}_y q_x), \quad (8.6)$$

²Just like position and momentum are conjugate variables related by Fourier transforms, the $|j\rangle$ and $|l\rangle$ basis are related by a discrete Fourier transform.

with spin orbit coupling strength given by $\alpha = \hbar^2 k_L / 2$. The zeroth-order Hamiltonian has continuous rotational symmetry while the proposed ring coupling only has discrete rotational symmetry. The symmetry of the Hamiltonian is recovered when higher order corrections are added to the Hamiltonian. The complete expressions for the higher order terms for $N = 3$ and $N = 4$ can be found in [108], and they are reminiscent of quadratic and cubic Dresselhaus SOC [109]. The largest leading order term for the $N = 3$ case is inversely proportional to Ω so that this ring-coupling scheme results in a more ‘Rashba-like’ Hamiltonian as one goes to higher coupling strengths. Figure 4 shows level curves of the ground state eigenenergies of Equation 8.5 for $N = 3$ and $\bar{\phi} = 0$ for increasing Ω . At low Ω the dispersion has discrete rotational symmetry and is characterized by three local minima³. As Ω is increased the local minima start merging into each other and in the large Ω limit we recover the characteristic Rashba ring-like dispersion.

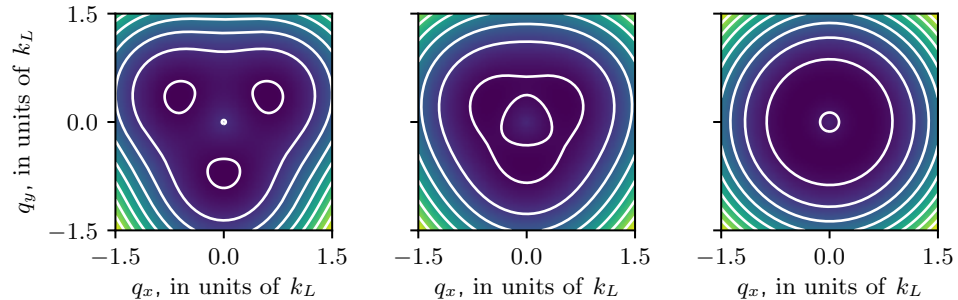


Figure 4: Ground state dispersion relation of Equation 8.5 for $N = 3$ and $\bar{\phi} = 0$ for $\Omega = 1.75 E_L$ (left), $\Omega = 3.5 E_L$ (middle) and $\Omega = 175 E_L$ (right). Higher order corrections to $\hat{H}^{(0)}$ decay as $1/\Omega^2$ and in the large Ω limit we recover the Rashba ring dispersion.

8.3 Experimental implementation of Rashba SOC

We implemented the ring-coupling scheme and thereby engineered Rashba SOC by resonantly coupling the $|xyz\rangle$ states from Chapter 6 states using two-photon Raman transitions [46] as depicted in Figure 5. The engineered system consisted of an effective spin-1/2 Rashba subspace, along with a topologically trivial high-energy branch. Our engineered Rashba system had a single Dirac cone near $\mathbf{q} = 0$, where the two lower dispersion branches become degenerate and the Berry curvature becomes singular. Each of these branches extend to infinite momentum, making the supporting manifold a plane rather than a torus. We characterized this system using both spectroscopy and quantum state tomography. This allowed us to measure the dispersion branches and directly observe the single Dirac point linking the lowest

³An alien face?



two branches as well as to reconstruct the Berry connection to derive the associated Chern numbers.

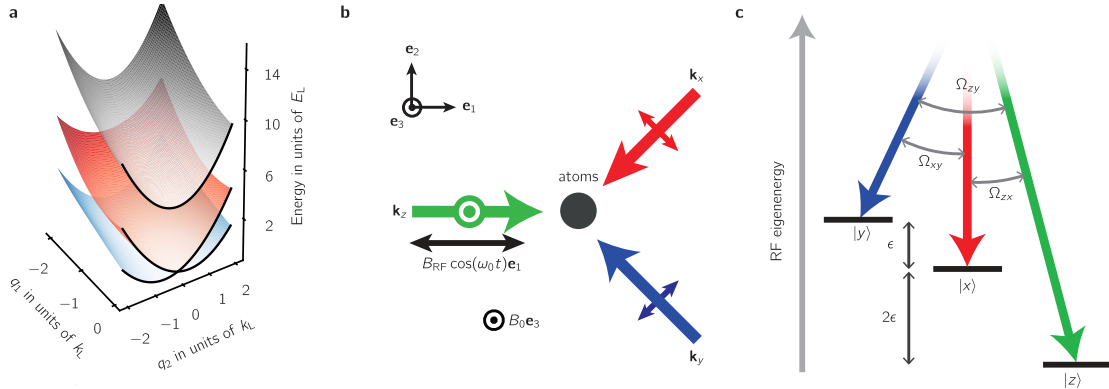


Figure 5: **a** Our engineered dispersion consisted of a two-level Rashba subspace (red and blue) with a single Dirac point linking the lowest two branches and a topologically trivial higher branch (gray). **b** We generated $|xyz\rangle$ states by combining a bias magnetic field along \mathbf{e}_3 with an RF magnetic field oscillating along \mathbf{e}_1 . These states were coupled by three cross-polarized Raman laser beams propagating along \mathbf{e}_1 , $\mathbf{e}_2 - \mathbf{e}_1$ and $-\mathbf{e}_1 - \mathbf{e}_2$. **c** Each pair of Raman lasers was in two-photon resonance with a single transition between the $|xyz\rangle$ states which we coupled strengths $(\Omega_{zx}, \Omega_{xy}, \Omega_{yz})/2\pi = (12.6(5), 8.7(8), 10(1))$ kHz.

All of our experiments started with about $N \approx 1 \times 10^{687}$ Rb atoms in a crossed optical dipole trap [110], with frequencies $(f_1, f_2, f_3) \approx (70, 85, 254)$ Hz, just above the transition temperature for Bose-Einstein condensation. We initially prepared the atoms in the $|F = 1, m_F = -1\rangle$ state of the $5S_{1/2}$ electronic ground state and transferred atoms to the $m_F = 0$ and $m_F = +1$ states as needed using ARP. A bias field $B_0 \mathbf{e}_3$ gave a $\omega_0/2\pi = 23.9$ MHz Larmor frequency along with a quadratic shift of $\epsilon/2\pi = 83.24$ kHz. The RF field used to generate the $|xyz\rangle$ states and implementing CDD had strength $\Omega_{RF} = 1.41(2)\epsilon$. We adiabatically prepared the $|xyz\rangle$ states starting from the m_F states following the procedure described in Section 6.4.

8.3.1 Raman coupling the $|xyz\rangle$ states

We Raman-coupled atoms prepared in any of the $|xyz\rangle$ states using the three cross-polarized Raman laser beams shown in Figure 5b, tuned to the ‘magic zero’ wavelength $\lambda_L = 790$ nm. We arranged the Raman lasers into the tripod configuration shown in Figure 5c, bringing each pair into two-photon resonance with a single transition with strengths $(\Omega_{zx}, \Omega_{xy}, \Omega_{yz})/2\pi = (12.6(5), 8.7(8), 10(1))$ kHz. The geometry of our experimental implementation differs from [46] where all Raman lasers are perpendicular. We had to go away from the ideal configuration because we

needed all of the Raman recoil vectors to lie on the imaging plane (spanned by \mathbf{e}_1 and \mathbf{e}_2) in order to image all the Raman induced \mathbf{k} dependent dynamics. As a result of this the dispersion relation no longer has discrete rotational symmetry, however the Dirac point is still present in our system. The only way to break the degeneracy of this system is to change the phase $\bar{\phi}$ and for our laser configuration we always have $\bar{\phi} = 0$.

The energies of the $|xyz\rangle$ states are $\omega_x = 0$ and $\omega_{z,y} = -(\epsilon \pm \sqrt{4\Omega_{\text{RF}}^2 + \epsilon^2})/2$. We set the frequencies of the Raman lasers to $\omega_x = \omega_L + \omega_0 + \omega_{xy}$, $\omega_y = \omega_L + \omega_0$ and $\omega_z = \omega_L - \omega_{zx}$, where $\omega_L = 2\pi c/\lambda_L$ and $(\omega_{zx}, \omega_{xy}, \omega_{zy})/2\pi = (166.47, 83.24, 249.71)$ kHz are the transition frequencies between pairs of dressed states and are integer multiples of ϵ for our coupling strength $\Omega = \sqrt{2}\epsilon$.

The Raman coupled states can be described by the combined kinetic and light-matter Hamiltonian

$$\hat{H}_{\text{R}}(\mathbf{k}) = \sum_{j \in \{xyz\}} \left(\frac{\hbar^2 k^2}{2m} + \hbar\omega_i \right) |j\rangle \langle j| + \sum_{j' \neq j} \hbar\Omega_{j,j'} e^{i(\mathbf{k}_{j,j'} \cdot \mathbf{x} - i\omega_{j,j'} t)} |j\rangle \langle j'|, \quad (8.7)$$

where $\mathbf{k}_{j,j'}$ is the recoil momentum from an $|j\rangle \rightarrow |j'\rangle$ transition and Ω_{ij} is the Raman coupling strength between a pair of RF dressed states. The Hamiltonian above only includes the matrix elements associated to resonant couplings. We apply the unitary transformation $\hat{U}_{j,j'} = \exp(-i\mathbf{k}_j \cdot \mathbf{x} - \omega_j t)\delta_{j,j'} |j\rangle \langle j'|$ so that the Hamiltonian takes the familiar form of the ring coupling scheme

$$\hat{H}_{\text{R}} = \sum_{j \in \{xyz\}} \left(\frac{\hbar^2(\mathbf{q} - \mathbf{k}_j)^2}{2m} + \hbar\delta_j \right) |j\rangle \langle j| + \sum_{j \neq j'} \hbar\Omega_{jj'} |j\rangle \langle j'|, \quad (8.8)$$

where \mathbf{k}_j are the Raman wave vectors and δ_j is the detuning from Raman resonance.

This coupling scheme simultaneously overcomes three limitations of earlier experiments [111, 112] that performed the ring coupling using states in both $5S_{1/2}$ hyperfine manifolds of ${}^{40}\text{K}$: (1) working in the same hyperfine manifold eliminates spin-relaxation collisions [113]; (2) unlike m_F states, the $|xyz\rangle$ states can be tripod-coupled with lasers far detuned relative to the excited state hyperfine splitting greatly reducing spontaneous emission [70]; and (3) CDD renders the $|xyz\rangle$ states nearly immune to magnetic field noise.

8.3.1.1 Floquet and off resonant coupling effects

We operated in a regime where the transition energies between the $|xyz\rangle$ states were integer multiples of ω_{xy} : $\omega_{zx} = 2\omega_{xy}$ and $\omega_{zy} = 3\omega_{xy}$, and therefore we can use Floquet theory for a complete description of our system [114]. We observed that the effective Raman coupling strengths for the driven three level system differed from our calibrations which were performed looking at Rabi oscillations from individual pairs of lasers because of the presence of nearby quasi-energy manifolds and off resonant coupling terms. This effect could be mitigated for larger values of ω_{xy} as the spacing between quasi-energy manifolds is increased and the off resonant coupling terms less

relevant. Appendix ?? has a full derivation of the Raman Hamiltonian starting from the $|m_F\rangle$ basis in the lab frame including the full time dependence and off resonant coupling terms.

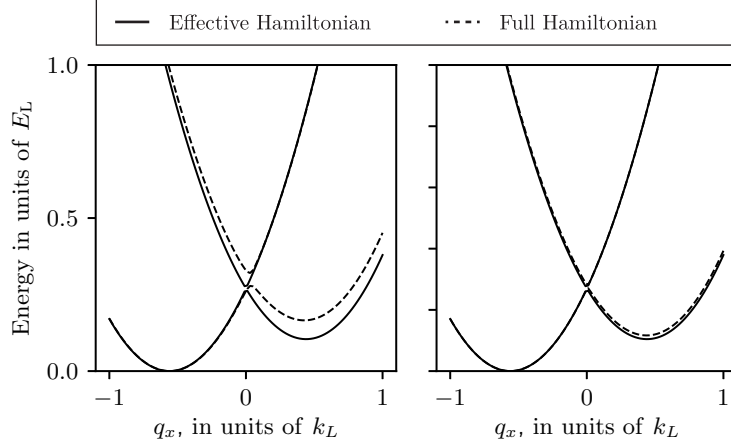


Figure 6: Solid lines: Dispersion relation from RWA Hamiltonian (Equation 8.8) as a function of q_x for $\Omega_{i,j} = 1.5 E_L$ and $\delta_i = 0$. Dashed lines: Dispersion relation computed for the full Floquet Hamiltonian. We considered $\omega_{zx} = 2\omega_{xy}$ and $\omega_{zy} = 3\omega_{xy}$ in both cases so the separation between Floquet manifolds is ω_{xy} . In the left panel $\omega_{xy} = 83.24$ kHz as in our experiments and in the right panel $\omega_{xy} = 416.2$ kHz. As the spacing between Floquet manifolds becomes we get a better agreement between the spectra of the RWA and Floquet Hamiltonians.

8.3.1.2 Lifetime

The limited lifetime due to spontaneous emission has always been a concern for Raman coupled systems. This was in part one of the reasons why we pursued the topology direction rather than trying to measure a fragile many-body phase. The measured spontaneous emission limited lifetime of our system was 320(17) ms, measured with the Raman lasers applied to the $|m_f\rangle$ states. However, it was reduced to 40(2) ms when we Raman coupled the $|xyz\rangle$ states, which we attribute to technical noise in the relative phase between the RF dressing field and the Raman laser fields, which has caused considerable consternation in ongoing experiments. All the experiments reported here were short compared to this timescale so this decreased lifetime was not an issue but it is a limitation that needs to be addressed in future experiments. Figure 7 shows measurements of the lifetimes of Raman dressed atoms in both $|m_f\rangle$ and $|xyz\rangle$ states. We obtained the lifetime by fitting decaying exponentials to the integrated OD obtained from absorption images of thermal atoms where the Raman was turned on in 1 ms and held on for up to 50 μ s⁴.

⁴How long we could hold on the Raman was limited by the RF antenna heating up.

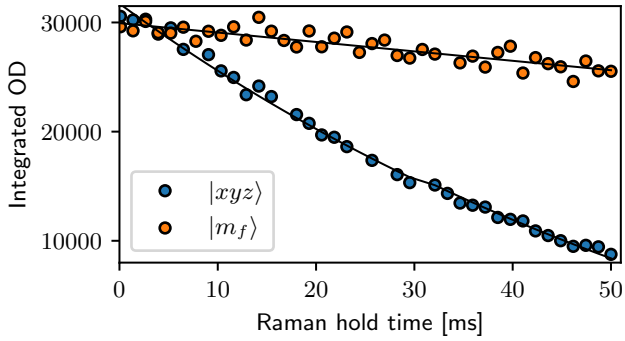


Figure 7: Lifetime of Raman dressed states. We Raman dressed atoms in the $|m_f\rangle$ and $|xyz\rangle$ states. The orange markers correspond to atoms initially prepared in $|m_f = -1\rangle$ (no high power RF involved) and the blue markers correspond to atoms $|xyz\rangle$ (three averaged traces). The lifetime of doubly dressed states is significantly reduced as compared to the lifetime of the Raman dressed $|m_f\rangle$ states, indicating that resonant scattering of photons is not our only loss mechanism.

8.3.2 Measuring quasimomentum distributions

Each pair of Raman lasers coupled states $|i, \mathbf{k}\rangle \rightarrow |j, \mathbf{k} + \mathbf{k}_{i,j}\rangle$ where $|i\rangle$ and $|j\rangle$ denote the initial and final $|xyz\rangle$ states, \mathbf{k} is the initial momentum and $\mathbf{k}_{i,j} = \mathbf{k}_i - \mathbf{k}_j$ is the two-photon Raman recoil momentum. Dressed states with quasimomentum \mathbf{q} are comprised of three bare states $|j, \mathbf{k}\rangle$ with momentum $\mathbf{k} = \mathbf{q} - \mathbf{k}_j$. The eigenstates of our Rashba SOC Hamiltonian take the form

$$|\Psi_n(\mathbf{q})\rangle = \sum_{j \in xyz} \sqrt{a_{n,j}(\mathbf{q})} e^{i\phi_{n,j}(\mathbf{q})} |j, \mathbf{k} = \mathbf{q} - \mathbf{k}_j\rangle, \quad (8.9)$$

where the quasimomentum \mathbf{q} is a good quantum number and the amplitudes are parametrized by $a_{n,j}(\mathbf{q})$ and $\phi_{n,j}(\mathbf{q})$. We leveraged the wide momentum distribution of a non-condensed ensemble ($T \approx 180$ nK and $T/T_c \approx 1.1$) to sample a wide range of momentum states simultaneously. By starting separately in each of the $|xyz\rangle$ states we sampled the range of quasimomentum states shown in Figure 8b, where the momentum distributions of an initial state $|j, \mathbf{k}\rangle$ is shifted from $\mathbf{q} = 0$ by the corresponding Raman wave vector \mathbf{k}_j .

Our measurement protocol consisted of abruptly removing the confining potential and the Raman lasers, initiating a 21 ms TOF. During this TOF we adiabatically transformed each of the $|xyz\rangle$ states back to a corresponding $|m_F\rangle$ state following the procedure described in Section 6.4 and spatially separated them using a Stern-Gerlach gradient. Finally we used resonant absorption imaging to measure the resulting spin-momentum distributions.

The FWHM of the cloud after TOF is about $700 \mu\text{m}$ which is much larger than the size of the in-situ cloud $\sim 50 \mu\text{m}$ and therefore the spatial density distribution

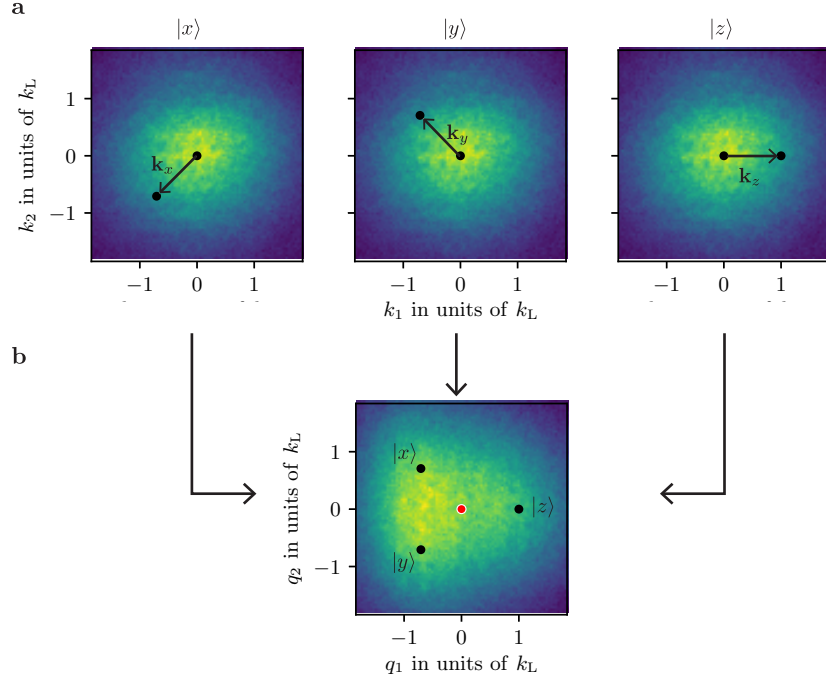


Figure 8: Mapping momentum into quasimomentum: **a** We used non-condensed atoms with a broad momentum distribution ($T \approx 180$ nK and $T/T_c \approx 1.1$). **b** Atoms in $|j, \mathbf{k}\rangle$ are mapped to Raman dressed states with quasimomentum $\mathbf{q} = \mathbf{k} + \mathbf{k}_j$. The black dots in the bottom panel represent the location of $\mathbf{k} = 0$ for each of the $|xyz\rangle$ states and the red dot corresponds to $\mathbf{q} = 0$. We performed our experiments starting separately in each of the $|xyz\rangle$ states, which allowed us to sample a larger range of quasimomentum states.

of the TOF images represents momentum distribution of the atoms. For the $7.4\text{ }\mu\text{m}$ pixel size of our camera and the 3.283 magnification of our imaging system, the momentum resolution of our images was $0.018\text{ }k_L$ and the momentum distribution of a single state measured after TOF had a FWHM of $\sim 2.2\text{ }k_L$.

8.3.2.1 Correcting shears from Stern-Gerlach gradient

The magnetic field gradient used to separate the different m_f states in TOF additionally creates a trap for atoms in the direction perpendicular to the Stern-Gerlach separation, causing a compression (expansion) of the $m_f = -1$ (+1) states (see Section 3.2.1). The faster moving atoms are subject to a stronger potential and therefore the projections of a given momentum state \mathbf{k} along the Stern-Gerlach axis and perpendicular to it were transformed as $k_{\parallel} \rightarrow k_{\parallel}$ and $k_{\perp} \rightarrow (1 + \alpha)k_{\perp}$, where $\alpha = 0$ for $m_f = 0$ and $\text{sign}(\alpha) = \pm 1$ for $m_f = \pm 1$.

Since we were interested in mapping the momentum distribution of atoms it was important for us to quantify and correct the effect of these shears in the TOF

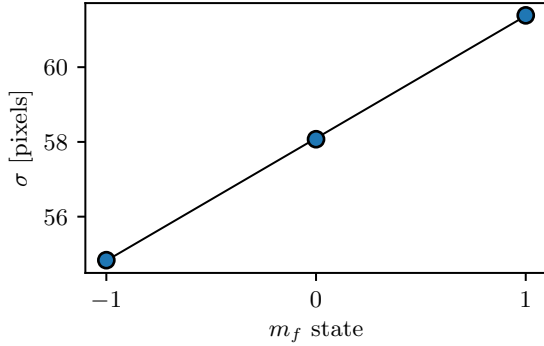


Figure 9: We measured the standard deviation of the momentum distribution along the axis perpendicular to the SG for 10 shots on each m_f state. From the slope of the linear fit we obtain a shearing parameter $\alpha \approx \pm 0.067$ for $m_f = \pm 1$.

images. We used two different methods: First we prepared thermal atoms in all three of the m_f states and fit 2D Gaussians rotated by the angle of the SG displacement; 63.8 degrees for our images. Figure 9 shows the standard deviation extracted from the Gaussian fits along the axis perpendicular to the SG deviation as a function of m_f state. We performed a linear fit of σ and found that the $m_f = \pm$ states are expanded/contracted by about $\pm 6.7\%$ size of the compared to the $m_f = 0$ cloud ($\alpha = \pm 0.067$).

Alternatively we performed the Ramsey interferometer described in Section 8.5 but coupling only 2 states, either $|z\rangle \leftrightarrow |x\rangle$ or $|x\rangle \leftrightarrow |y\rangle$ (mapped to $| -1 \rangle \leftrightarrow | 0 \rangle$ and $| 0 \rangle \leftrightarrow | +1 \rangle$ after TOF). We looked at the oscillation frequencies of the density for each pixel of the CCD camera (each sheared momentum state) and fit them to Equation 8.17 for fixed value of the recoil momentum $\mathbf{k}_{i,j}$ and with a free shear parameter that modifies \mathbf{q} . Using this method we extracted a shearing of the order of 7%, in good agreement with the Gaussian fitting method.

The transformed momentum coordinates were described by a function

$$g(\mathbf{k}) = (k_{\parallel}, (1 + \alpha)k_{\perp}) \quad (8.10)$$

and our observed data $(y_i^{(\text{shear})}, \mathbf{k}^{(\text{shear})})$ was the density in the sheared coordinate system at the i th pixel of the CCD sensor. The density in the unsheared coordinate was estimated using

$$y_j = \frac{\sum_i \exp[-(g(\mathbf{k}_j) - \mathbf{k}_i^{(\text{shear})})^2 / 2\sigma^2] y_i^{(\text{shear})}}{\sum_i \exp[-(g(\mathbf{k}_j) - \mathbf{k}_i^{(\text{shear})})^2 / 2\sigma^2]}, \quad (8.11)$$

where σ is the spacing between two consecutive pixels ($\sim 0.018 k_L$). Prior to any data analysis we applied this transformation to all of our images, where we used different values of α that define $g(\mathbf{k})$ for each of the m_f states.

8.4 Fourier spectroscopy of the Rashba dispersion

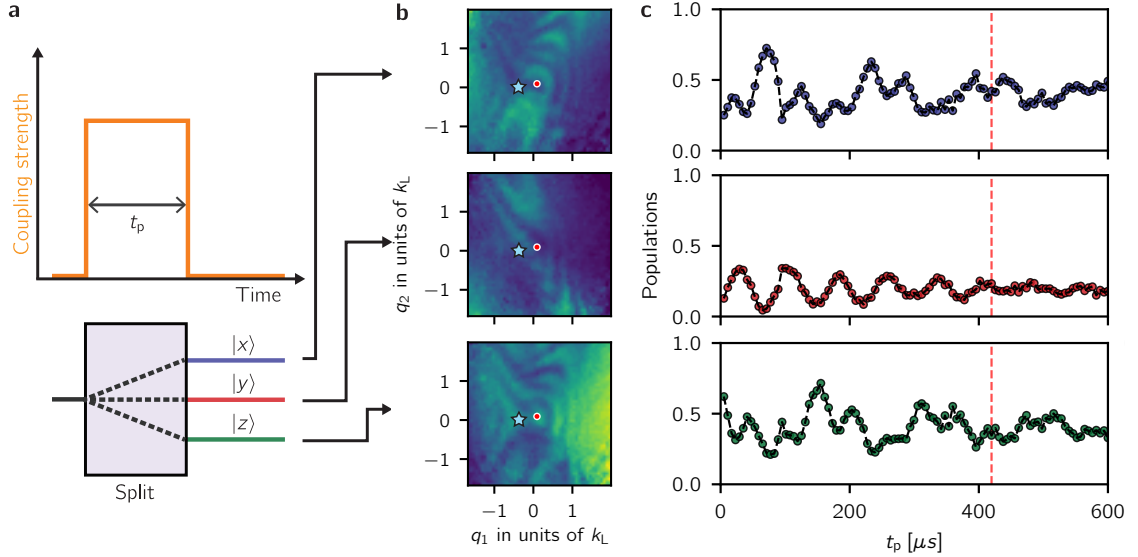


Figure 10: **a** Fourier spectroscopy protocol. We applied the Raman lasers for a variable time t_p : a Rabi-type atomic interferometer analogous to a three-port beam splitter. **b** Probabilities as a function of quasimomentum for a fixed Raman pulse time $t_p = 420 \mu s$ **c** Dynamics of the final populations of the $|xyz\rangle$ states with quasimomentum $(q_1, q_2) = (-0.55, -0.18) k_L$ (blue star in panels **b**) after initializing the system in the $|z\rangle$ state.

We directly measured the 2D dispersion relation using Fourier transform spectroscopy [40]. We considered the evolution of an initial state $|i, \mathbf{k}\rangle$ suddenly subjected to the Raman coupling lasers. This atomic Rabi-type interferometer is analogous to the three-port beam-splitter depicted in Figure 10a. During a pulse time t_p we followed the dynamics of the populations in the $|xyz\rangle$ states which evolved with oscillatory components proportional to $\sum_{j \neq n} a_{n,j}(\mathbf{q}) \cos([E_n(\mathbf{q}) - E_j(\mathbf{q})]t_p/\hbar)$, with frequencies determined by the eigenenergy differences $E_n - E_j$. Figure 10b shows the momentum dependent populations for a fixed pulse time t_p and Figure 10c shows representative final populations as a function of t_p for a fixed quasimomentum state. We Fourier transformed the populations with respect to t_p and for a given quasimomentum state for a total of 9 state, all of them with the same \mathbf{q} accounting for each of the three initial $|xyz\rangle$ states that was then split into 3 states. Figure 11 shows the PSD computed for each of the 9 states for planes of constant q_1 . The amplitude of the oscillatory components depends on the overlap integral between the initial state and the Raman dressed states (see Equation 5.1) so sampling all these states gave us access to a wider range of measurable frequencies. The spectral maps in Figure 12b were produced by averaging the PSDs from the 9 different states using

\bar{n} , the mean population in t_p , as a weight:

$$\text{PSD}^{(\text{mean})}(\mathbf{q}) = \frac{\sum_{i,j} \text{PSD}_{i,j}(\mathbf{q}) \bar{n}_{i,j}(\mathbf{q})}{\sum_{i,j} \bar{n}_{i,j}(\mathbf{q})}, \quad (8.12)$$

where the indices i, j represent the different states of the grid shown in Figure 11. The extrema in the spectral maps are the energy differences $E_n - E_j$ in the engineered dispersion (Figure 10a). Figure 12 was obtained by combining all the spectral maps, and together they show the presence of a single Dirac point in the Rashba subspace, evidenced by the gap closing near $\mathbf{q} = 0$ and the photon-like lower branch. The dashed curves correspond to the energy differences computed for our system using the dispersions shown in Figure 12a, and are in clear agreement with our experiment. This measurement directly confirms the expected set of energies, including the existence of a two-state subspace approximately described by the Rashba Hamiltonian.

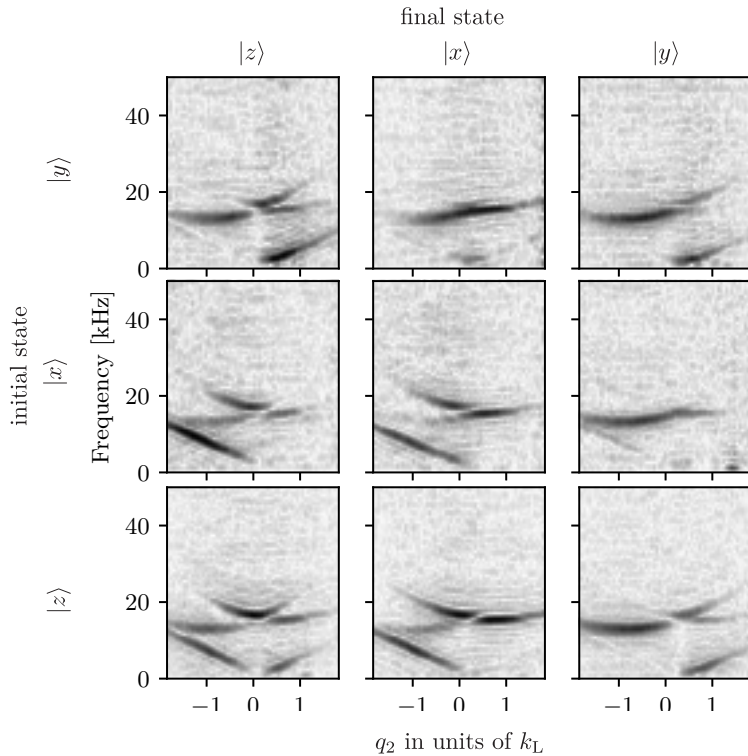


Figure 11: PSD of all the analyzed states as a function of q_2 for fixed $q_1 = 0.18 k_L$. The different overlaps between the initial state, the Raman dressed states and the measured final state result in peaks with different amplitudes.

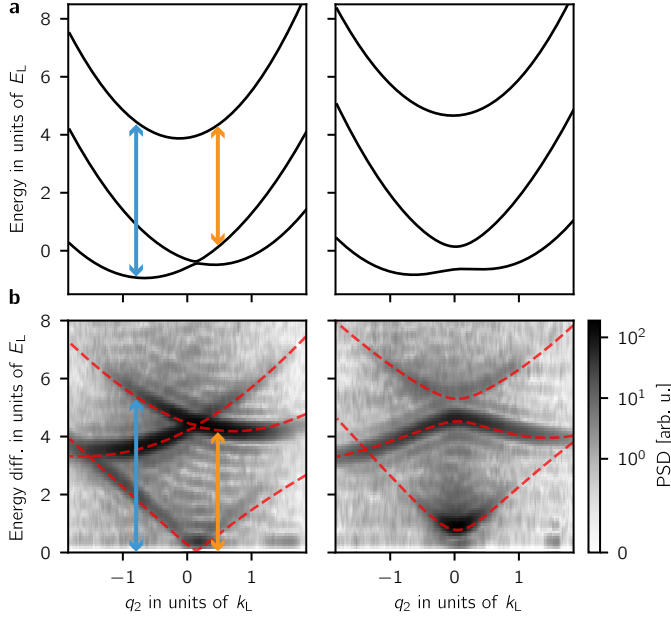


Figure 12: **a** Predicted dispersion relation as a function of q_2 for fixed $q_1 = -0.09 k_L$ (left) and $0.65 k_L$ (right), computed for the experiment parameters. The energy differences between the branches enclosing the vertical arrows appear as peaks in the spectral maps below. **b** Power spectral density (PSD) for the same parameters as above which we obtained by Fourier transforming the populations in the $|xyz\rangle$ states with respect to t_p . The dashed lines correspond to the energy differences computed using the dispersion curves on the top panel.

8.5 Quantum state tomography with Ramsey interferometer

The Fourier spectroscopy measurement confirmed our quantum engineering of the Rashba Hamiltonian. However, the energies shed no light on the topology of the different branches of the dispersion, which instead requires knowledge of the eigenstates. The Berry curvature present in the definition of the Chern number (Equation 7.11) can be derived from the Berry's connection $\mathbf{A}_n(\mathbf{q}) = i \langle \Psi_n(\mathbf{q}) | \nabla_q | \Psi_n(\mathbf{q}) \rangle$, which as discussed in Chapter 7 behaves much like a vector potential in classical electromagnetism. The Berry curvature $\Omega_n(\mathbf{q}) = \nabla_q \times \mathbf{A}(\mathbf{q})$ is the associated magnetic field and the flux through any surface is the line integral of $\mathbf{A}(\mathbf{q})$ along its boundary, after neglecting the contributions of Dirac strings which I will discuss later. Using the expression for the Raman dressed eigenstates from Equation 8.9 we obtain

$$\mathbf{A}_n(\mathbf{q}) = - \sum_{j \in \{x,y,z\}} a_{n,j}(\mathbf{q}) \nabla_q \phi_{n,j}(\mathbf{q}), \quad (8.13)$$

which depends on both the phase and amplitude of the wave function. We obtained $a_{n,j}(\mathbf{q})$ and $\phi_{n,j}(\mathbf{q})$ using a three-arm time-domain Ramsey interferometer (see Section 3.5.2), implementing a variant of quantum state tomography [115, 116]. The

use of a multi-path interferometer allowed us to transduce information about phases into state populations, which we readily obtained from absorption images.

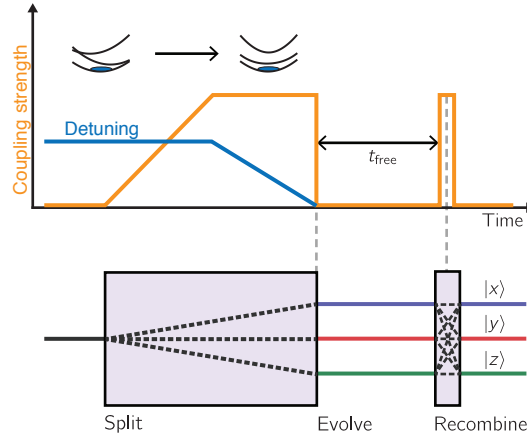


Figure 13: Experimental protocol for three-arm Ramsey interferometer (not to scale). (Top) We started with atoms in state $|z, y, \mathbf{q}_i = \mathbf{k} + \mathbf{k}_j\rangle$ and with detuning $\delta_y = \pm 5 E_L$ and $\delta_z = \pm 5 E_L$. We ramped the Raman lasers on in $750 \mu\text{s}$ and then ramped the detuning to nominally zero. We let the system evolve in the dark for times between $5 \mu\text{s}$ and $400 \mu\text{s}$, followed by a $25 \mu\text{s}$ Raman pulse. (Bottom) The implemented experimental protocol was equivalent to a three-arm interferometer that split an initial state into three final states with amplitudes related to the initial wave function phases.

Figure 13 shows our experimental protocol which I will describe in more detail in the following section. We adiabatically mapped an initial $|j, \mathbf{k}\rangle$ state into a corresponding eigenstate $|n, \mathbf{q} = \mathbf{k} + \mathbf{k}_j\rangle$, either in the topologically trivial highest dispersion branch ($n = 3$) or in the topological ground branch ($n = 1$) by dynamically tailoring both the Raman coupling strength and detuning. We suddenly turned off the Raman coupling, thereby allowing the three bare state components of the Rashba eigenstates to undergo free evolution for a time t_{free} , constituting the three arms of our time-domain interferometer. Finally we applied a three-port beam splitter using a brief Raman ‘recombination’ pulse to interfere the three arms.

8.5.1 Wave function evolution in Ramsey interferometer

Rashba dressed state preparation: We started with $|xyz\rangle$ states at different RF coupling strength $\Omega_0 = \Omega_{\text{RF}}/\pi 2 \pm 20 \text{ kHz}$, such that the energies of the $|z\rangle$ and $|y\rangle$ states were shifted by about $\pm 18.8 \text{ kHz}$. We used the same Raman frequencies as described earlier and therefore the change in the $|xyz\rangle$ state eigenenergies corresponded to non-zero δ_z and δ_y in Equation 8.8. We chose the detuning such that the initial state had a large overlap with either the $n = 1$ or the $n = 3$ eigenstates of Equation 8.8. We then ramped on the Raman coupling in $750 \mu\text{s}$, adiabatically

mapping the $|z\rangle$ and $|y\rangle$ states into the $n = 1$ or $n = 3$ eigenstates. Because our only experimental knob for dynamically changing the detuning was Ω_{RF} we could not control δ_x so when we initialized the system in $|x\rangle$ the final dressed state always corresponded to the $n = 2$ branch. After turning on the Raman we ramped Ω_{RF} to its final value in 1 ms, effectively ramping δ_z and δ_y close to zero. This detuning ramp had the additional effect of moving the location Dirac point through the atoms when loaded in the $n = 1$ branch, thereby creating a trajectory where the state preparation was not adiabatic. This trajectory depended on the sign of the detuning ramp so we combined data from different initial states in order to exclude the Dirac point trajectories. Near the final location of the Dirac point the state preparation can not be adiabatic regardless of the initial state or detuning used for the ground state preparation. Figure 14a shows an example an absorption image of atoms initially prepared in the $|y\rangle$ state and with δ_y such atoms are loaded in the $n = 1$ branch. The Dirac point is initially located near the lower left edge of the cloud and when δ_i was ramped the location of the Dirac point was dragged across the whole cloud leaving lines where non-adiabatic transitions occurred as can be seen in Figure 14b. The location of the Dirac point as a function of δ_i can also be directly computed by numerically diagonalizing the SOC Hamiltonian from Equation 8.8. At the end of this stage, excluding the points of non-adiabatic transitions, the state of the system was described by the eigenstates in Equation 8.9.

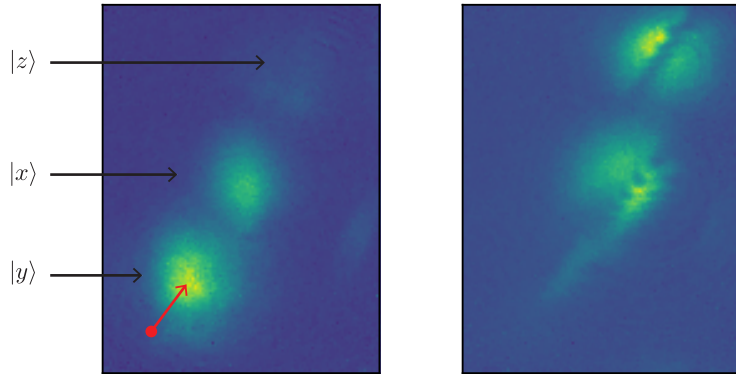


Figure 14: **a** We prepared atoms in the $|y\rangle$ state such that they are adiabatically mapped to the ground dispersion branch. **b** We ramped δ_i and dragged the Dirac point through the atoms.

Free evolution: We suddenly turned off the Raman coupling, thereby projecting the Raman dressed states back into the $|xyz\rangle$ basis. Each of the $|xyz\rangle$ state represents a different branch of the interferometer and they acquire phases that are proportional to t_{free}

$$|\Psi_n(\mathbf{q})\rangle \rightarrow \sum_{j \in xyz} \sqrt{a_{n,j}(\mathbf{q})} e^{i\phi_{n,j}(\mathbf{q})} e^{-iE_j(\mathbf{q})t_{\text{free}}/\hbar} |j, \mathbf{k} = \mathbf{q} - \mathbf{k}_j\rangle, \quad (8.14)$$

where $E_j(\mathbf{q}) = \hbar^2 \mathbf{q}^2 / 2m$ is the free particle energy. The Rashba wavefunction phases $\phi_{n,j}(\mathbf{q})$ that we were interested in measuring were imprinted during the loading procedure. The dynamical phases $E_j(\mathbf{q})t_{\text{free}}/\hbar$ acquired in the different interferometer arms does not contribute to our knowledge of the Rashba eigenstates as they describe the evolution of the system in the absence of Raman dressing.

Recombination pulse: We applied a 25 μs Raman pulse that acted as a second beam splitter in our interferometer sequence. The wave function after the pulse is

$$|\Psi(\mathbf{q})\rangle = \sum_{j,j' \in xyz} \sqrt{a_{n,j}(\mathbf{q})} e^{i(\phi_{n,j}(\mathbf{q}) - E_j(\mathbf{q})t_{\text{free}}/\hbar)} U_{j,j'}(\mathbf{q}) |j, \mathbf{k} = \mathbf{q} - \mathbf{k}_j\rangle, \quad (8.15)$$

where $U_{j,j'}(\mathbf{q}) = |U_{j,j'}(\mathbf{q})| \exp(i\phi_{j,j'}^{(\text{pulse})}(\mathbf{q}))$ is the matrix element of the unitary transformation $\exp(i\hat{H}_{\text{R}}(\mathbf{q})t_{\text{pulse}})$ associated to the Raman pulse. At the end of this procedure, the population in a final state $|l, \mathbf{q}\rangle$ is

$$P_l(\mathbf{q}, t) = \sum_{i \neq j} |U_{l,i}| |U_{j,l}| \sqrt{a_{n,i} a_{n,j}} \cos(\omega_{i,j}(\mathbf{q})t + \phi_{n,i}(\mathbf{q}) - \phi_{n,j}(\mathbf{q}) + \phi_{l,i,j}^{(\text{pulse})}(\mathbf{q})), \quad (8.16)$$

which directly reads out the phase differences, independent of the output port l . Here $\phi_{l,i,j}^{(\text{pulse})}(\mathbf{q})$ is a smoothly varying phase imprinted by the recombination pulse and is independent of \mathbf{q} in the limit of short, strong pulses and does not affect the topological index of the system. The angular frequencies

$$\omega_{i,j}(\mathbf{q}) = \hbar \mathbf{q} \cdot \mathbf{k}_{i,j} / m + \delta_{i,j} \quad (8.17)$$

result from the known free particle kinetic energy, the recoil momenta and detuning $\delta_{i,j}$ from the tripod resonance condition. Figure 13b shows the momentum-dependent populations in each output port at fixed $t_{\text{free}} = 160 \mu\text{s}$ and Figure 13c shows the populations as a function of t_{free} for a representative quasimomentum state $(q_1, q_2) = (0.55, -0.92) k_{\text{L}}$.

We obtained the relative phases $\Delta\phi_{n,i,j,l}(\mathbf{q}) = \phi_{n,i}(\mathbf{q}) - \phi_{n,j}(\mathbf{q}) + \phi_{l,i,j}^{(\text{pulse})}(\mathbf{q})$ from Equation 8.16 by fitting the measured populations to the sum of three cosines with the known free particle frequencies but unknown amplitudes and phases.

8.5.2 Combining phases from different measurements

We combined the phases $\Delta\phi_{n,i,j,l}(\mathbf{q})$ obtained from fits to six different states (two initial states split into 3 states). Similar to the Fourier spectroscopy measurements, we performed a weighted average of the fitted relative phases

$$\Delta\phi_{n,i,j}(\mathbf{q}) = \frac{\sum_l \Delta\phi_{n,i,j,l}(\mathbf{q}) w_{i,j,l}(\mathbf{q})}{\sum_l w_{i,j,l}(\mathbf{q})}, \quad (8.18)$$

where the weights are determined using fit uncertainties and when loading atoms in the topological branch we additionally accounted for the trajectory of the Dirac point

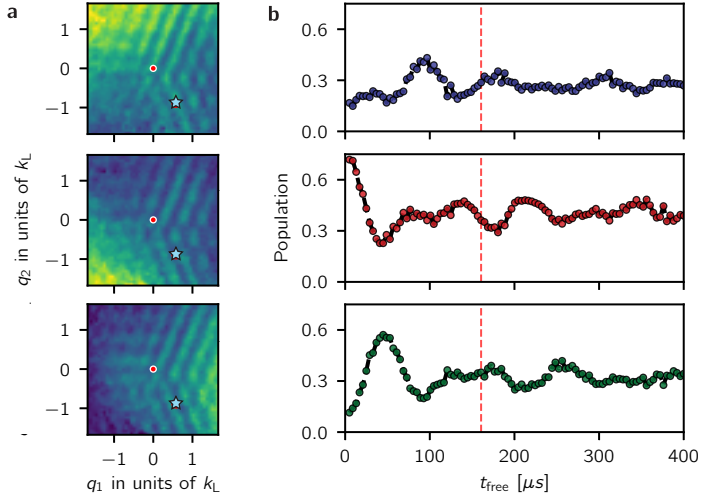


Figure 15: **a** Probabilities as a function of quasimomentum for the three output ports of the interferometer at $t_{\text{free}} = 160 \mu\text{s}$ **b** Probabilities as a function of free evolution time t_{free} for an input state with quasimomentum $(q_1, q_2) = (0.55, -0.92) k_L$ indicated by the blue star on **a** and in the topological ground branch ($n = 1$)

during the loading procedure. Figure 16 shows an example of two different weight arrays used to combine the phase difference associated to the $z \rightarrow x$ transition $i, j = z, x$ for the topological branch $n = 1$ ($\Delta_{1,z,x}$):

The ‘spokes’ in the weight arrays correspond to high uncertainty regions. This uncertainty comes of our inability to resolve the phases of low frequencies $\omega_{ij}(\mathbf{q})$ as well as when two different frequencies $\omega_{ij}(\mathbf{q})$ and $\omega_{i'j'}(\mathbf{q})$ are close to each other which is limited by the largest value of t_{free} in the experiment. I fit and combined a total of 120,000 different time traces (60,000 for each dispersion branch) to produce phase maps like those shown in Figure 17a.

8.5.3 Measuring the topological index

Figure 17a shows typical phase-maps for both the non-topological and topological branches. In the non-topological phase-maps the momentum dependence of the recombination pulse $\phi_{l,i,j}^p(\mathbf{q})$ causes a smooth variation of the phases along the Raman recoil axes that does not affect the evaluation topological index of our system. We recovered the phases $\phi_{n,j}$ of the full spinor wave function from the relative phases $\Delta\phi_{n,i,j}(\mathbf{q})$ by choosing a particular gauge such that $\phi_{n,3} = 0$. We then used the values of $a_{n,i}$ obtained from measuring the populations in the $|xyz\rangle$ states at $t_{\text{free}} = 0$ in combination with the phases of the wave function to compute the Berry connection [117]. Figure 17b shows the three phase differences as a function of polar angle for a loop of radius $q \approx 0.77 k_L$. In addition to the smooth variations induced by the recombination which are present in both columns, the phases of the topological branch have two π valued jumps that lead to non-zero Berry phases when the

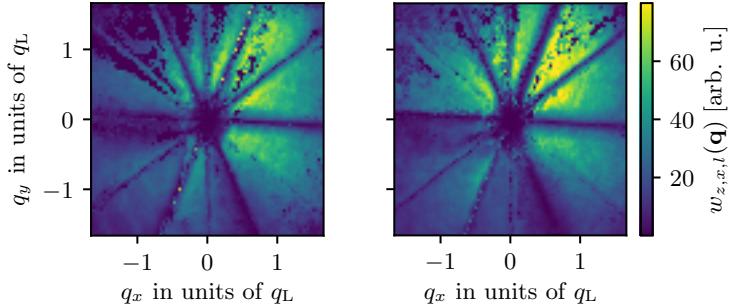


Figure 16: Two sample weight arrays $w_{i,j,l}(\mathbf{q})$ for $i, j = z, x$ and atoms prepared in the topological disperion branch. We obtained the weights using the uncertainties from the fits and the trajectory of the Dirac point during the state preparation. We combined the weights and the phase differences $\Delta\phi_{n,i,j,l}$ obtained from the time dependent fits using Equation 8.18 to obtain the phase maps displayed in Figure 17a

Berry connection is integrated along a closed loop in momentum space. Figure 17c shows the integrated Berry phase as a function of loop radius. As mentioned earlier the largest value of t_{free} limits how well we can resolve the phases of small frequencies and this is reflected in the large variation in the Berry phase depicted in the shaded region of Figure 17c near $q = 0$. For loops with $q > 0.4 k_L$ we obtain an integrated Berry phase that suggests an asymptotic Chern number of $\Phi_B/2\pi = 0.01(1)$ for the non-topological branch and $\Phi_B/2\pi = 0.5(5)$ for the topological branch. However, Berry's phase measurements including ours includes the (potential) contribution of any Dirac strings traversing the integration area. In our system, these are possible at the Dirac point *, and each contributes $\pm 2\pi$ to Φ_B as was discussed in Section 7.6. Even with this 2π ambiguity we are able to associate a half-integer Chern number with the topological branch, which is possible only for a topological dispersion branch in the continuum.

8.6 Conclusion

In conventional lattices — for example graphene, or the topological Haldane model — it is well established that Dirac points each contribute a Berry's phase of $\Phi_B/2\pi = \pm 1/2$ [118], but crystalline materials conspire for these to appear in pairs [119], always delivering integer Chern numbers. In contrast, our continuum system contains a single Dirac point, resulting in a non-integer Chern number. This leads to intriguing questions about edge states at interfaces with non-integer Chern numbers with non-integer Chern number differences. Initial studies in the context of electromagnetic waveguides [120] and atmospheric waves [77] have applied Chern invariants and the bulk-edge correspondence to continuous media.

While the true Rashba Hamiltonian features a ring of degenerate eigenstates, our implementation including the quadratic and cubic Dresselhaus-like SOC lifts

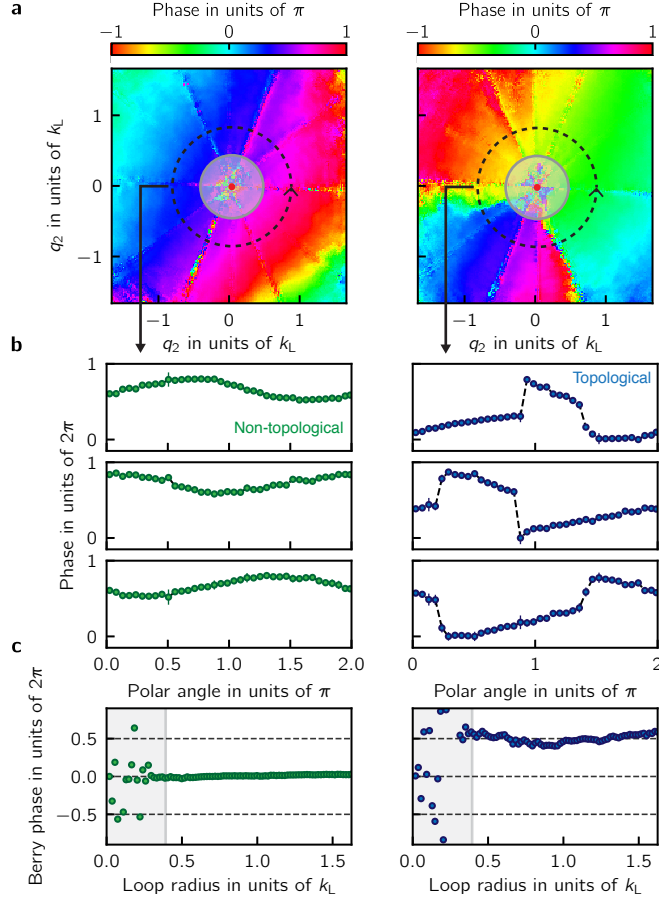


Figure 17: Topological invariants from quantum state tomography, for the non-topological branch ($n = 3$, left) and the topological branch ($n = 1$, right). **a** Phase differences as a function of quasimomentum from the the $z \rightarrow x$ transition **b** Phase differences as a function of polar angle for a loop radius $0.77 k_L$ from the $z \rightarrow x$ (top), $x \rightarrow y$ (middle) and $y \rightarrow z$ (bottom) transitions. The phases associated to the topological branch are characterized by two π valued discontinuities. Each row of phases was shifted by a constant value so that the three rows of phases share the same vertical axis. All phases shown here were binned and averaged using the fit uncertainties as weights. **c** Inferred Chern number as a function of loop radius. For loops with $q > 0.4 k_L$ we obtained an integrated Berry phase and asymptotic Chern number of $\Phi_B/2\pi = 0.01(1)$ for the non-topological branch and $\Phi_B/2\pi = 0.5(5)$ for the topological branch.

this macroscopic degeneracy giving three nearly degenerate minima [108]. Already these three minima could allow the study of rich ground state physics in many body systems of bosons, for example the formation of fragmented BECs [104] when the system does not condense into a single-particle state. Furthermore, the use of additional spin states or larger Raman couplings can partially restore this degeneracy allowing the possible realization of fractional Hall like states [121].